Master's thesis

Correlated lateral phase separations in stacks of lipid membranes

(邦題):積層脂質膜における相分離の連動性 (英文)

Supervisor: Associate Professor Shigeyuki Komura

Department of Chemistry, Graduate School of Tokyo Metropolitan University

Student ID: 14880328

Name: Takuma Hoshino

Date: January 8, 2016

Abstract

Summary of Master Dissertation
(Master Program (Science))

14880328 Takuma Hoshino

Correlated lateral phase separations in stacks of lipid membranes
（邦題）： 積層脂質膜における相分離の連動性（英文）

A biological membrane is regarded as a two-dimensional fluid sheet composed of mainly amphiphilic phospholipids. A phospholipid molecule typically has a hydrophilic part called as a head group, and a hydrophobic part called as a tail. Biological membranes are constructed out of two monolayers (leaflets) arranged in back-to-back configurations, where the head groups in both monolayers face with a water-rich environment and are stabilized by the water molecules. Biomembranes are mainly composed of phospholipids but contain also other molecules such as cholesterol, glyco-sugars and proteins. In living organisms, these membranes can form not only plasma membranes but also multi-lamellar stacks known as lamellar bodies. Examples of such highly folded membranous structures are thylakoid membranes of photosynthetic cyanobacteria or plant chloroplasts, and stratum corneum of human skin. Since multilamellar structures can combine single membrane functions in series, they offer possibilities for novel applications in photonics and as bio-sensors.

Although many researches on artificial vesicles mimicking the role of cell membranes have been performed, there are only a few studies on artificial multi-lamellar membranes. Motivated by the experimental study of Tayebi *et al.* [*Nature Mater.* **11**, 1074 (2012)] on phase separation of stacked multi-component lipid bilayers, we propose a model composed of stacked two-dimensional Ising spins. Whereas the Ising spin model is generally applied for magnetic systems, it can be also used to describe the phase separation between the two components even if there is no magnetization.

We study both its static and dynamical features using Monte Carlo simulations with Kawasaki spin exchange dynamics that conserves the order parameter. We show that at thermodynamical equilibrium, due to strong inter-layer correlations, the system forms a continuous columnar structure for any finite interaction across adjacent layers. This observation reproduces the columnar structure reported in the experiments on stacked membranes.

Furthermore, the phase separation shows a faster dynamics as the inter-layer interaction is increased. This result is also in accord with the experimental observation of the domain growth dynamics in the same reference as above. This temporal behavior is mainly due to an effective deeper temperature quench because of the larger value of the critical temperature, $T_{\rm c}$, for larger inter-layer interaction. When the temperature ratio, $T/T_{\rm c}$, is kept fixed, the temporal growth exponent does not increase and even slightly decreases as function of the increased inter-layer interaction.

The present investigation has revealed that our simple model based on the Ising model can describe the correlated lateral phase separations in stacks of lipid membranes. Our model is universal and can be applied to study various phenomena occurring in multi-lamellar membranes as well as their rich functions.

Contents

Chapter 1

Introduction

1.1 Biological membranes

A biological membrane is regarded as a two-dimensional sheet composed of mainly amphiphilic phospholipids. A phospholipid molecule has a hydrophilic part called as head group, and a hydrophobic part called as tail. Biological membranes are constructed out of two monolayers (leaflets) arranged in back-to-back configurations, where the head groups in both monolayers face with a water-rich environment and are stabilized by water molecules, as shown in Fig. 1.1. Biomembranes are mainly composed of phospholipids but contain also other molecules such as cholesterol, glyco-sugars, and proteins [1].

It is known that the membranes can form various types of bilayer strucrure corresponding to the living environments. The most well-known membrane is a plasma membrane which defines the boundary between inside and outside of the cell. Plasma membranes play an important role to adjust the amount of the components, pH and osmotic pressure within the cell. In living organisms, these membranes can form not only a plasma membrane but also multi-lamellar stacks known as lamellar bodies [2]. Examples of such highly folded membranous structures are thylakoid membranes of photosynthetic cyanobacteria or plant chloroplasts, and stratum corneum of human skin. Since multilamellar structures can combine sin-

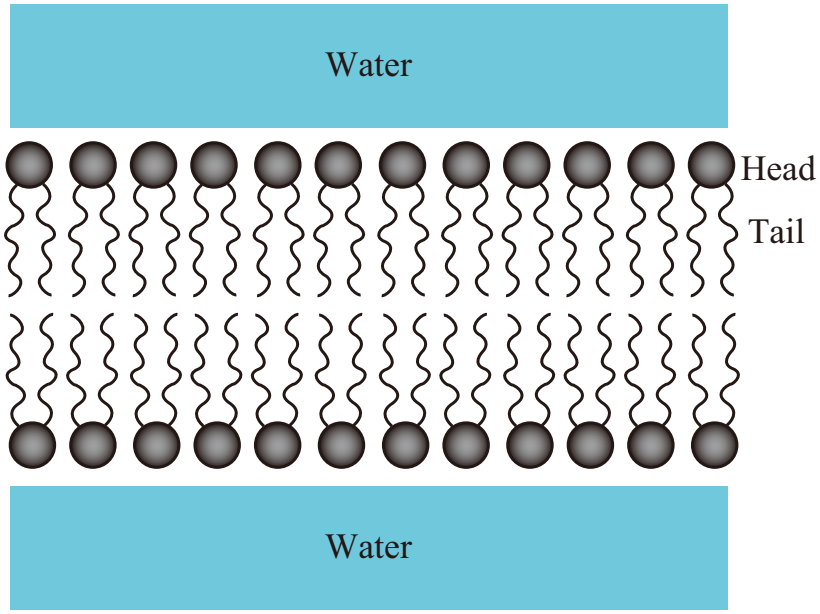

Figure 1.1: Schematic image of a lipid bilayer. Because phospholipids have amphiphilicity, monolayers form back-to-back configurations, where the head group in both monolayers faces with a water-rich environment and is stabilized by the water molecules.

gle membrane functions in series, they offer possibilities for novel applications in photonics and as bio-sensors.

1.2 Major lipids in cell membranes

Lipid molecules constitute about 50 % of the mass of most animal cell membranes, nearly all of the remainder being proteins. All of the lipid molecules in cell membranes are *amphiphilic* which means that the molecule has both a hydrophilic and a hydrophobic part in its body.

The most typical membrane lipid is a phospholipid. In a phospholipid, there are a polar head group and two hydrophobic carbon tails. One carbon tail has at least one *cis*-double bond, while, the other tail has no double bond. Because at least one tail has an unsaturated hydrocarbon bond, phospholipids are generally

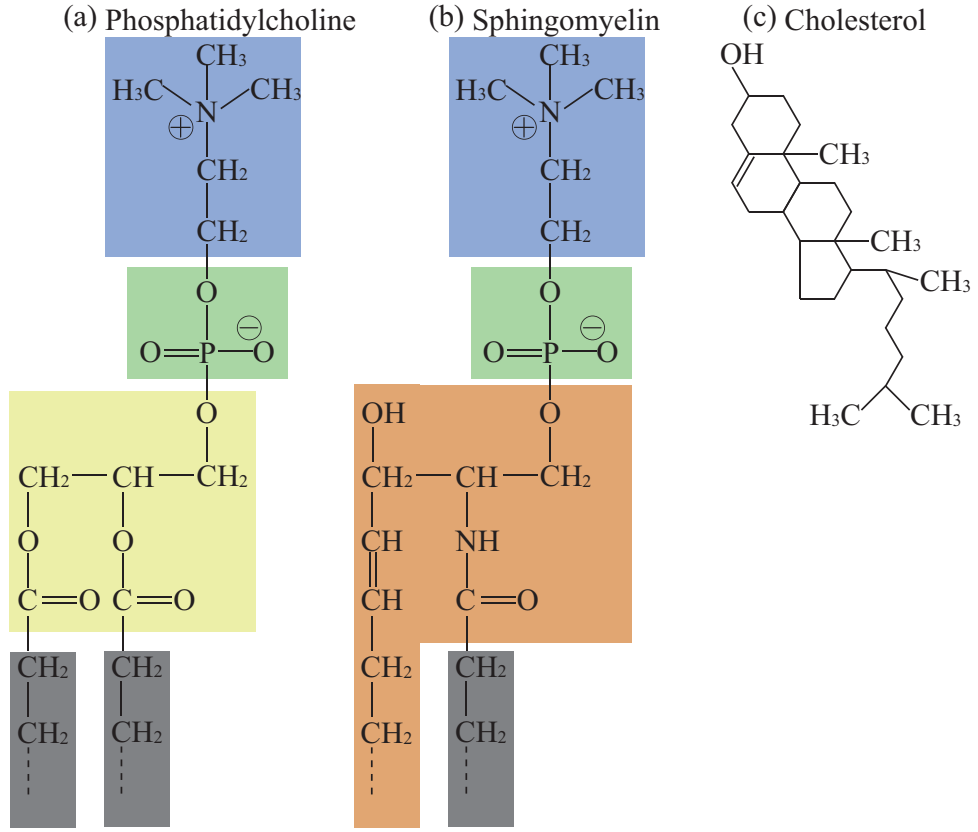

Figure 1.2: Chemical structure of phospholipids. (a) Phosphatidylcholine. The yellow, green and blue regions represent glycerol group, phosphate and choline, respectively. (b) Sphingomyelin. The orange region represents sphingosine. (c) Cholesterol. Cholesterol has a rigid ring structure with a short hydrocarbon chain and a hydroxyl group at the terminal.

classified into *unsaturated lipids*.

A typical phospholipid is a *phosphoglyceride* which has a three-carbon *glycerol* backbone. Two fatty acids are linked through ester bonds to adjacent two carbon atoms of the glycerol, and the third carbon atom is linked to a phosphate group which contains several different types of head group. Examples are ethanolamine $NH_3^+(CH_2)_2OH$, serine $NH_3^+CH(COO^-)CH_2OH$, and choline $N^+(CH_3)_3CH_2CH_2OH$. In Fig. 1.2(a), a phosphatidylcholine is shown.

Another important phospholipid is a *sphigolipid* which is built from sphingosine

instead of glycerol. Sphingosine has also a three-carbon backbone such as glycerol, although the structure is different from glycerol. Sphingosine is a long acyl chain with an amino group at the middle of the three carbon atoms and two hydroxy groups at the other carbon atoms. In sphingolipids, a fatty acid group is attached to the amino group, and a phosphate is linked to the terminal hydroxyl group, leaving one hydroxyl group free. This free hydroxyl group can contribute to the polar properties of the adjacent head group. In addition, the fatty acid group of a sphingomyelin is typically saturated. Hence sphingolipids are regarded as saturated lipids in cell membranes. In Fig. 1.2(b), a sphingomyelin is shown.

In addition, many plasma membranes contain *choresterol*. Cholesterol has a rigid ring structure with a short hydrocarbon chain and a hydroxyl group at the terminal, as shown in Fig. 1.2(c). Cholesterol plays an important role in lipid membranes to adjust the fluidity.

1.3 Bilayer structure of lipid membranes

Lipids spontaneously form a bilayer strucrure due to the amphiphilicity. Lipid membranes consist of two monolayers (leaflets) arranged in a back-to-back configurations, where the head groups in both monolayers face with a water-rich environment and are stabilized by the water molecules. This stable structure prevent water molecules from penetrating freely, which is very important for plasma membranes to adjust the concentration of ions. An example of a bilayer structure is a *vesicle* (called liposome in biology) shown in Fig. 1.3. The bilayer in vesicles forms a closed spherical structure. This closed structure is physically stable because it avoids the exposure of the hydrophobic tails to water, which would be energetically unfavorble.

In living organisms, biological membranes can form not only a plasma membrane but also multi-lamellar stacks known as lamellar bodies. Examples of such highly folded membranous structures are thylakoid membranes of photosynthetic cyanobacteria or plant chloroplasts, and stratum corneum of human skin. Since

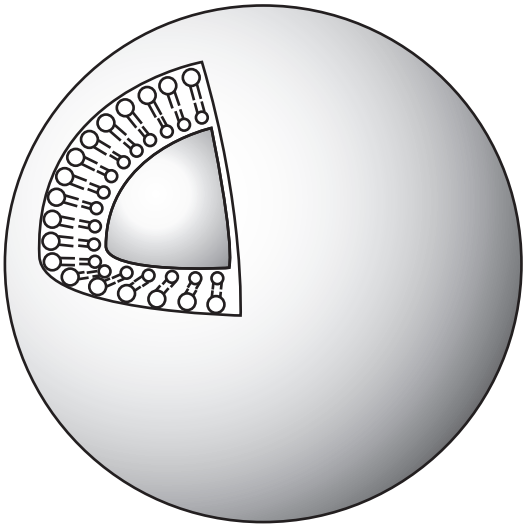

Figure 1.3: Bilayer structure of a vesicle. The closed strucure is stable because it avoids the exposure of the hydrophobic hydrocarbon tails to water, which is energetically unfavorble.

multilamellar structures can combine single membrane functions in series, they offer possibilities for novel applications in photonics and as bio-sensors.

1.4 Fluidity of membranes

The biomembranes of animal cells rapidly change shape as the cells move. These rapid changes in shape suggest that the plasma membrane itself is fluid, rather than rigid in character. Such a freedom of movement was demonstrated by Frye and Edidin in 1970. They fused two cells labbeled with different fluorescent tags on proteins and, showed that tags spread and the intermixing occured after membrane fusion [3]. This result indicates that the lipids can be regarded as a fluid.

In a lipid bilayer, there are many thermal motions, as shown in Fig. 1.4. For example, lipid molecules readily exchange places with their neighbors within a monolayer ($\sim 10^7$ times per second). This gives rise to a rapid lateral diffusion. In contrast, the process known as "flip-flop" (the exchange of lipid molecules between the two leaflets, $10^{-4} \sim 10^1$ times per second) occurs slower than the lateral

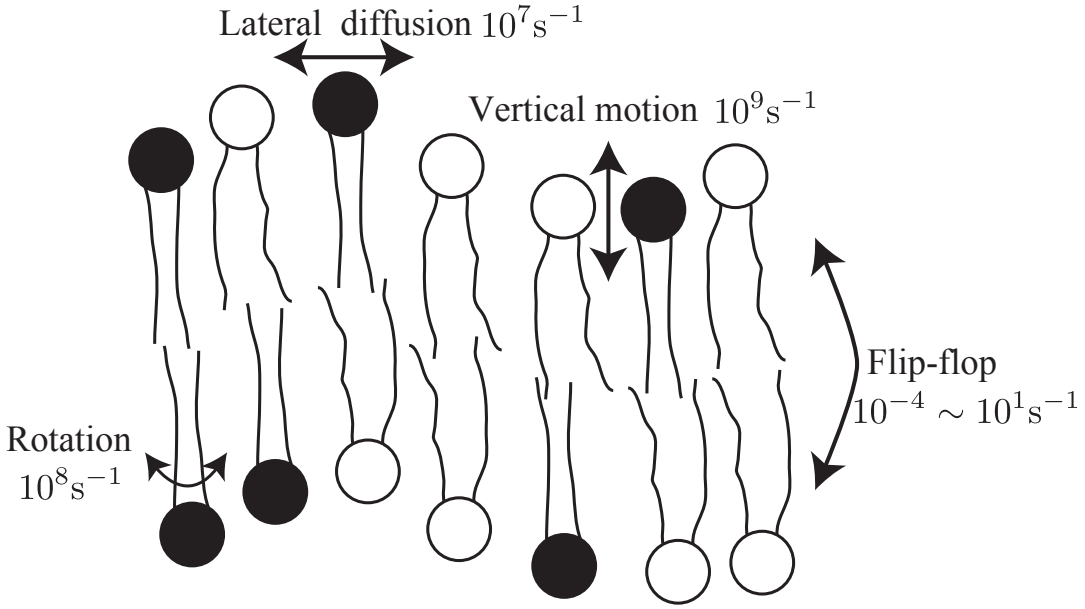

Figure 1.4: Thermal motion of a lipid bilayer. Lateral diffusion ($\sim 10^7$ time per second), fllip-flop motion ($10^{-4} \sim 10^1$ time per second), rotation ($\sim 10^8$ time per second) and vertical motion ($\sim 10^9$ time per second) occur in a lipid bilayer. These motions give rise to the fuidity of a bilayer membrane.

movement. In addition, rotation ($\sim 10^8$ times per second) and vertical motion ($\sim 10^9$ times per second) occur as well. A lipid bilayer has a fluidity because of these movements.

The model called *Fluid-Mosaic Membrane Model* (F-MMM) was proposed by Singer and Nicolson in 1972 [4] based on the thermodynamics principals of organization of membrane lipids and proteins, and available evidences of asymmetry and lateral mobility within the membrane matrix. Models proposed before F-MMM did not take into account the ability of components in membranes to rapidly move laterally and dynamically and change their distributions. The F-MMM regard biological membranes as a matrix made up of a mostly fluid bilayer of phospholipids with mobile globular integral membrane proteins and glycoproteins that are intercalated into the fluid lipid bilayer. The F-MMM has been known to describe the dynamic phenomena such as lateral diffusion of the membrane proteins in

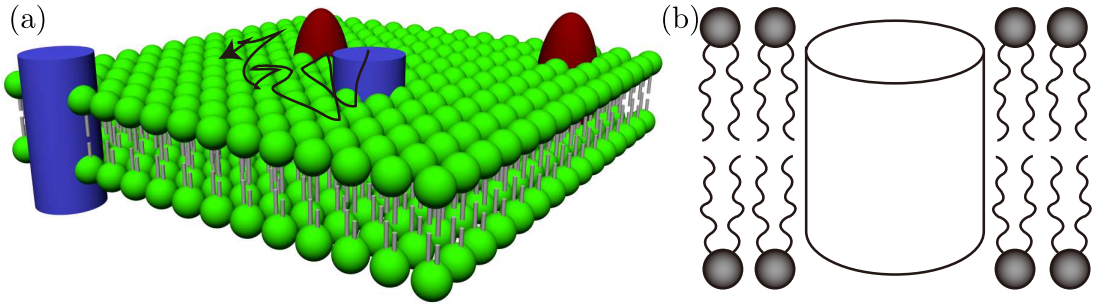

Figure 1.5: (a) A lipid bilayer and proteins (blue and red) are represented. Biological membranes are composed of not only phospholipids but also other molecules and proteins. (b) Illustration of a membrane protein within a lipid bilayer. The protein is regarded as a cylinder moving in the bilayer undergoing Brownian motion.

living cell. In Fig. 1.5, proteins within the lipid bilayer are represented. A protein is regarded as a cylinder moving in the bilayer under the action of Brownian motion [5].

In F-MMM, lipids and membrane proteins diffuse under thermodynamical motions. However, there is an enrichment of amine- and serine-containing phospholipids found on the cytoplasmic surface (inner surface), and choline-containing phospholipids and sphingomyelins on the outer surface of the cell membrane. In addition, they can be also unevenly and dynamically distrubuted in the monolayer. Certain lipids change the fluidity, dynamics and lateral structures of cell membranes. The activity of sterol such as cholesterol and certain lipids in biological membranes is particularly important in the formation of membrane domains called "raft" domains.

1.5 Artificial membranes

Ternary lipid mixtures consisting of cholesterol (Chol), sphingomyelin (SM), and unsaturated phospholipids are of considerable interest as models for lipid rafts, which are thought to be relevant in a variety of cell-surface signaling in biological membranes [6, 7, 8, 9]

Over the last decade, many studies have been performed on artificial giant unilamellar vesicles (GUVs) composed of ternary mixtures of saturated lipid such as SM (sphingomyelin), unsaturated lipid such as DOPC (1,2-dioleoyl-sn-glycero-3-phosphocholine) and cholesterol [10, 11]. By decreasing temperature, these ternary mixtures undergo a lateral phase separation, where a liquid-disordered (L_d) phase coexists with a liquid-ordered (L_o) one. It is known that the L_o phase is rich in saturated lipid and cholesterol, while the L_d phase is rich in the unsaturated lipid.

1.6 Stacked membranes

In a recent experimental study, Tayebi *et al.* [12] reported that a stack (typically composed of several hundred layers) of multicomponent lipid bilayers with phase-separated domains exhibits inter-layer columnar ordering. Using ternary mixtures of sphingomyelin, DOPC and cholesterol, it was observed that domains in stacked bilayers align one on top of the other, thereby forming an uninterrupted columnar ordering across hundreds of bilayer membranes.

This columnar structure in stacked membranes is shown in Fig. 1.6. Such a cooperative multilayer epitaxy was attributed to the interplay between intra-layer domain growth and inter-layer coupling.

As far as the dynamics of phase separation in stacks of membranes is concerned, the temporal evolution of the average inplane domain size, R, was shown to obey a power-law growth, $R \sim t^{\alpha}$ with $\alpha \approx 0.455$, as shown in Fig. 1.7. This exponent is larger than the value obtained using GUVs with a single bilayer, for which the reported experimental value is $\alpha \approx 0.28 \pm 0.05$ [13]. Hence, Tayebi *et al.* concluded that membrane stacking not only causes inter-layer correlation, but also accelerates the inplane domain growth in each of the bilayers.

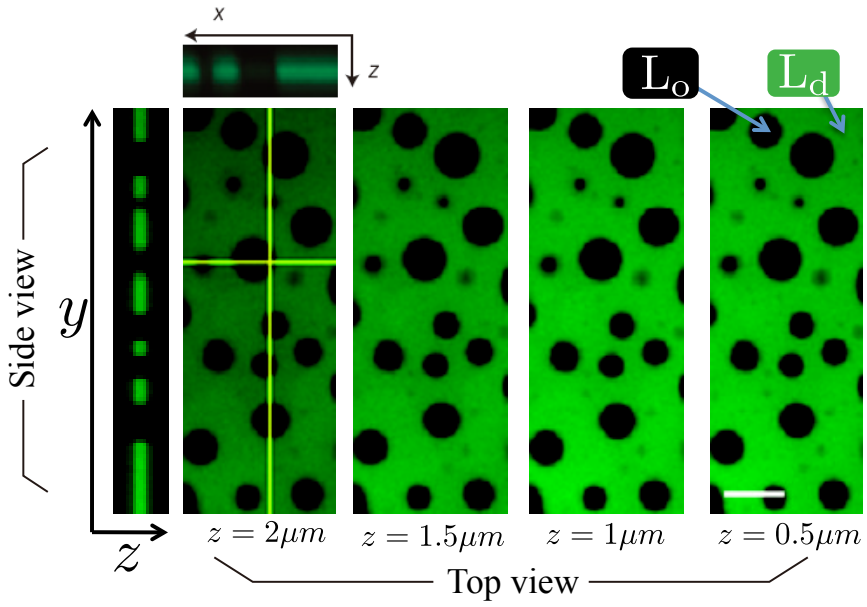

Figure 1.6: Depth-resolved confocal fluorescence microscopy of aligned stacked lipid bilayers. Membrane multilamellae consisting of (1:1 SM/DOPC + 30%Chol) at 30% relative humidity, doped with 0.1 mol% *N*-lissamine rhodamine palmitoyl phosphatidylethanolamine (Rho-PE). Some arbitrarily selected layers (z-slice) are represented. Each z-slice whose depth from the substrate is different has same domain positions. The side views for (depth $z = 2.0\mu m$) show the cross-section view along the yellow-colorured path, indicating near-complete three-dimensional alighnment of domains. The sample thickness is estimated to be $2.5 \pm \mu m$ by confocal microscopy, representing approximately 417 ± 83 layers. This indicates that domains in stacked bilayers align one on top of the other, thereby forming an uninerrupted columnar ordering across hundreds of bilayer membranes [12].

1.7 Aim of this thesis

In a subsequent paper [14], a model based on regular solution theory, which takes into account the inter-lamellar coupling of inplane phase-separated domains, was proposed. The calculated phase diagram was presented in terms of intra-layer and inter-layer coupling parameters, and contains three different regions: (i) a "one-phase" region in which the system does not exhibit phase separation; (ii) a "two-phase" region in which two phases coexist and domains in different layers

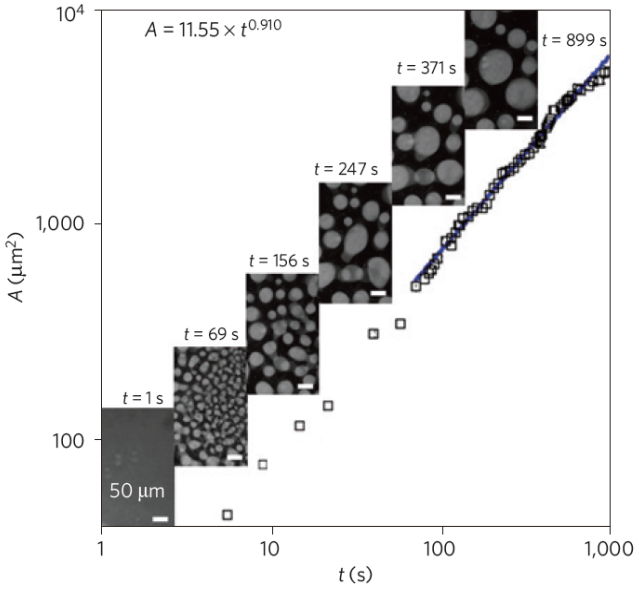

Figure 1.7: Domain evolution and coarsening. A presentative example of domain-size evolution in stacked lipid bilayers consisting of equimolar SM and DOPC at 30 % Cholesterol doped with Rho-PE in bulk water. Fitting domain size evolution to the universal growth law $\langle A \rangle \sim t^{2\alpha}$, yields $\alpha = 0.455$ for this example [12].

along the normal z-direction are completely aligned and have the same composition in the various layers, and (iii) a "multi-phase" region in which there are unaligned inplane domains with different composition in the different layers. According to Ref. [14], the transition line between the "two-phase" and "multi-phase" regions strongly depends on the number of layers in the stack which as varied up to ten layers.

Being motivated by these works [12, 14], we investigate the correlation between lateral phase separation in a stack of multi-layer membranes using a spin model called the *stacked two-dimensional (2d) Ising model* [15]. The model is the same as the *anisotropic three-dimensional (3d) Ising model* for a finite stack in the z-direction. The important difference between the two models is that in the former the order parameter (magnetization) in each layer is conserved. This requirement is based on the experimental fact that the A/B lipid composition in each layer

almost does not change during experimental times.

In our model, we study the thermodynamical equilibrium features using Monte Carlo (MC) simulations, and show that the domains in each layer are correlated along the vertical z-direction, for any finite value of the inter-layer interaction is positive, $J' > 0$. Hence, the system is either in a one- or two-phase state, and in our model the "multi-phase" state is not obtained in the thermodynamic limit of infinite lateral size, as long as the inter-layer coupling $J' > 0$. As anticipated, it is found that the phase-transition temperature, $T_{\rm c}(J')$, increases as function of the inter-layer interaction parameter. For any finite value of J', the critical temperature of the multi-layer stack interpolates between the values of the 2d and 3d Ising spin systems, $T_{\rm c}^{\rm 2d} < T_{\rm c}(J') < T_{\rm c}^{\rm 3d}$.

We also investigate the dynamics of phase separation at fixed temperature T in the two-phase coexistence region. We show that the accelerated temporal behavior of the phase separation for the stack is mainly driven by the increase of the temperature quench, $\Delta T = T_{\rm c}(J') - T$, because $T_{\rm c}(J')$ becomes larger for larger J'. However, if the ratio $T/T_{\rm c}(J')$ is kept fixed, the dynamics of the phase separation becomes even slower for larger values of the inter-layer coupling, J'.

In the next section, we describe the stacked 2d Ising model and review the MC simulation method. In Sec. 3, we present the equilibrium properties of the model, and discuss the condition for domain columnar ordering. Section 4 describes the dynamics of domain growth for different values of the inter-layer interaction, and it is compared with a previous theoretical work.

Chapter 2

Model and simulation technique

2.1 Stacked two-dimensional Ising model

In our simulations, we use the *stacked 2d Ising model*, shown in Fig. 2.1(a). We consider a stack of two-component lipid bilayer membranes composed of an A/B lipid mixture, although the experimental systems often consist of ternary lipid/-cholesterol mixtures. This simplification does not affect the essential feature of the lateral phase separation. Another simplification is that we treat only symmetric bilayers where the composition of the two leaflets is identical. Hence, each lipid bilayer having a finite thickness can be mapped into a 2d Ising model with conserved magnetization, expressing the fact that no lipid is allowed to exchange across layers. The 2d Ising layers are stacked in the z-direction, and they interact with their two nearest-neighboring layers, as depicted in Fig. 2.1(b).

The Hamiltonian of this stacked and coupled 2d Ising system can be written as:

$$H = -J \sum_{i,\langle \boldsymbol{\rho},\boldsymbol{\rho}'\rangle} S_{i,\boldsymbol{\rho}} S_{i,\boldsymbol{\rho}'} - J' \sum_{i,\boldsymbol{\rho}} S_{i,\boldsymbol{\rho}} S_{i+1,\boldsymbol{\rho}} - \sum_{i,\boldsymbol{\rho}} \mu_i S_{i,\boldsymbol{\rho}}, \tag{2.1}$$

where up/down values of the spin, $S_{i,\boldsymbol{\rho}} = \pm 1$, at $\boldsymbol{\rho} = (x, y)$ in the i-th layer corresponds to a lattice site occupied by an A or B lipids, respectively. The coupling

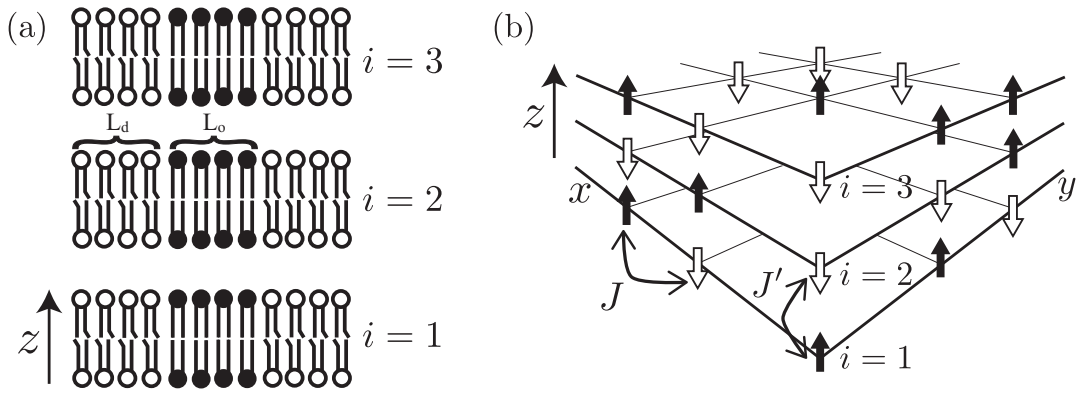

Figure 2.1: (a) Schematic illustration of a stack of binary membranes, taken here as a stack of three bilayers in the z-direction. Each bilayer is composed of two identical leaflets containing saturated lipids (A, black) and unsaturated lipids (B, white). Saturated and unsaturated lipids typically form L_o and L_d phases, respectively. As the lipid molecules are not allowed to exchange between different bilayers, their composition in each bilayer is fixed. (b) The stacked two-dimensional (2d) Ising model. Here the bilayer structure of each membrane is neglected. Lipid A and B correspond to spin up (black) and spin down (white), respectively. J is the coupling parameter between nearest-neighbor spins in the same layer, while J' is the coupling parameter between spins belonging to two nearest-neighboring layers.

between nearest-neighbor spins in the xy-plane (denoted by $\langle \boldsymbol{\rho}, \boldsymbol{\rho}' \rangle$) is J, while the coupling with the nearest-neighbor spins across layers in the z-direction is J'. The physical origin of the inter-layer interaction J' is primarily attributed to direct van der Waals attractive interactions acting between neighboring bilayers [16]. Other non-specific interactions, such as electrostatic and/or hydration interactions, can be taken into account through the second virial coefficient and will affect the value of J' as well [17, 18]. Throughout this thesis, we shall use the dimensionless ratio defined by $\lambda \equiv J'/J$ as a measure of the inter-layer coupling strength.

In the above Hamiltonian, μ_i is the external field (chemical potential), which fixes the average magnetization (A/B composition) in the i-th layer. Although μ_i can, in general, take different values for different layers, we consider here the case where all of them are the same, $\mu_i = \mu$, fixing the same value of lipid composition in all layers. This assumption holds also for the dynamical states since we do not allow

the lipids to be exchanged across different layers. The average order parameter (A/B composition) in the i-th layer is denoted by $\overline{S}_{i,\boldsymbol{\rho}}$, and throughout this thesis (except in Fig. 3.3(b) and in Sec. 4.4) we choose $\overline{S}_{i,\boldsymbol{\rho}} = 0$, which corresponds to a symmetric 1:1 A/B lipid mixture, *i.e.*, at the critical composition. This is equivalent to setting the value of the chemical potential to zero, i.e., $\mu = 0$.

The present model is related to the *anisotropic 3d Ising model* for a finite slab. The special case of $\lambda = 1$ corresponds to the isotropic 3d Ising model, whereas for $\lambda = 0$ the stack is composed of non-interacting 2d Ising layers. One interesting issue related to the anisotropic model, $0 < \lambda < 1$, is the crossover from 2d to 3d critical behavior [19] that will be explored below. We also note that the stacked 2d Ising model has been studied a great deal in connection with multilayer adsorption phenomena on attractive substrates [20, 21], but not in the context of layers of binary mixtures with conserved magnetization (order parameter) as studied in this thesis.

2.2 Monte Carlo simulation

We investigate both the statics and dynamics of a stack of membranes based on the Hamiltonian presented in Eq. (2.1). We employ MC simulations for classical Ising spins on a finite $L \times L \times L_z$ lattice. Periodic boundary conditions are used in all three directions. The spin configurations are updated using Kawasaki exchange dynamics [22] in order to conserve the magnetization in each layer. This is based on the experimental fact that lipids almost do not exchange across different layers. Hence, their A/B inplane composition is fixed during experimental times.

The MC simulations presented here are performed in the following way. At each MC trial step, a site on the 3d lattice and one of its nearest neighbors in the *same* layer are chosen at random. If the two spins are alike, a new site is again chosen at random. This process is repeated until two unlike nearest neighbor spins are found. Then, the probability of exchanging the two spins is determined by the standard Metropolis algorithm [23]. If the energy difference due to the spin

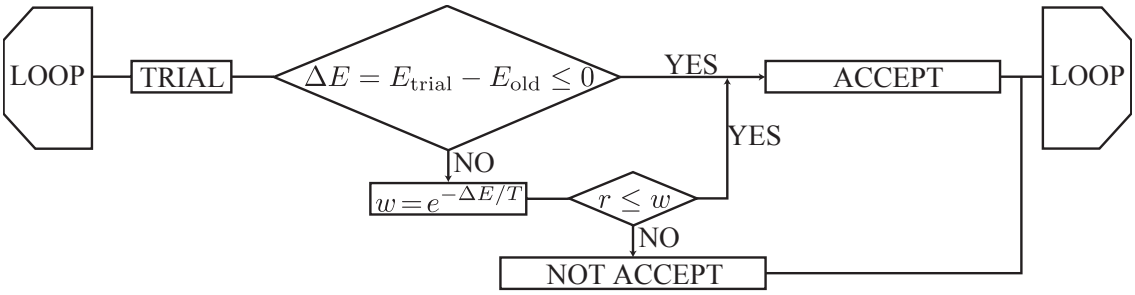

Figure 2.2: Metropolis algorithm.

exchange becomes negative, i.e., $\Delta E < 0$, we accept the exchange. Otherwise, we accept the exchange with a probability $\exp(-\Delta E/T)$, where T is the temperature and the Boltzmann constant, $k_{\rm B}$, was set to unity.

In one Monte Carlo step (MCS), this procedure is repeated $L \times L \times L_z$ times. The MC simulations are carried out by annealing the temperature gradually from an initial infinite temperature for which the spin configurations are completely disordered and uncorrelated. The first 10^5 (or in some cases up to 10^6) MCS are discarded in order to reach thermal equilibration. Furthermore, to avoid correlations between different equilibrated configurations, measurements are taken every 20 MCS, and we averaged over 10^5 independent system configurations, in order to obtain sufficient statistics.

In order to investigate the phase separation dynamics, we monitor the domain coarsening as a function of time (MCS) at a constant temperature below $T_{\rm c}$. An example of a typical time evolution of phase separation is presented in Fig. 2.3 for $\lambda = 0.1$, $T/J = 1.63$ and $L = L_z = 64$, where six snap-shots are shown from 10^2 MCS till 10^7 MCS. For clarity purposes, only the boundaries between domains of spin up (rich in lipid A) and spin down (rich in lipid B) are shown. In the initial time steps, the phase separation occurs inplane, andthe domains coarsen without much out-of-plane coupling (due to the rather small value of $\lambda = 0.1$). As time evolves, the inplane coarsening is also followed by out-of-plane columnar ordering, where the lipid A (and lipid B) rich domains are highly correlated along the z-

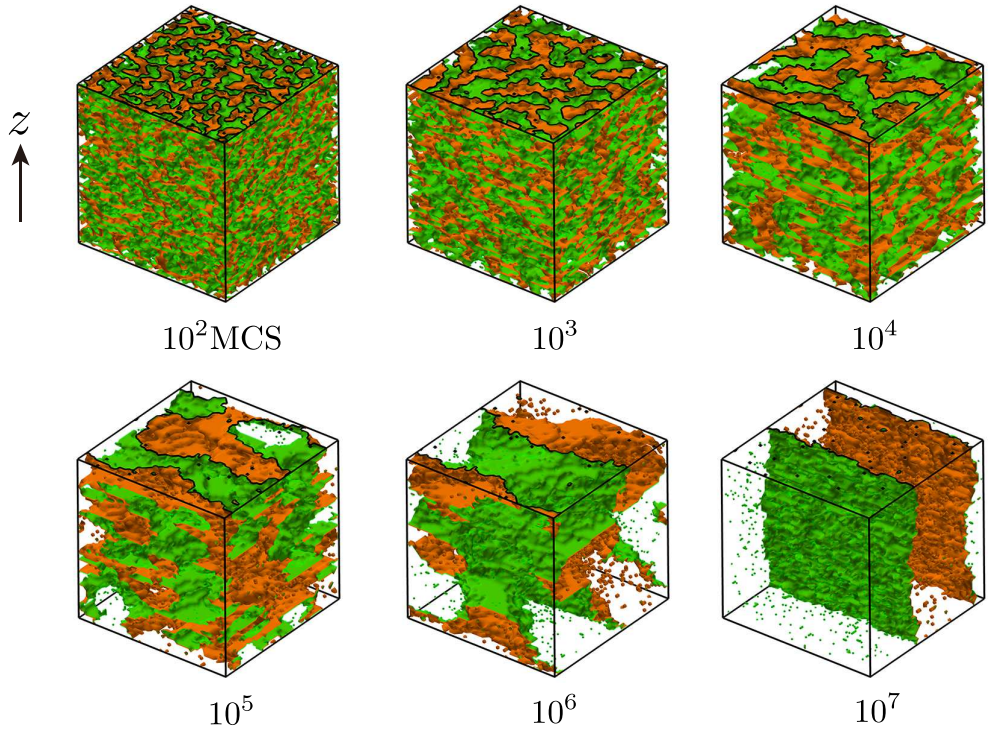

Figure 2.3: Time evolution of phase separated domains in the stacked 2d Ising model at different MC steps for $\lambda = 0.1$ and $T/J = 1.63$. The other parameters are $\overline{S}_{i,\boldsymbol{\rho}} = 0$ and $L = L_z = 64$. For presentation purposes, only the interfaces of domain boundaries are shown, and the two different sides of the interfaces are represented by green and brown. The system is fully equilibrated after about 10^7 MCS.

direction. This is clearly seen for the fully equilibrated configuration occurring after about 10^7 MCS (last snap-shot). Here the two color boundaries, represent the two sides of the domain boundaries (while the inside of the domain is not shown). The boundaries look like extended interfaces separating inplane domains that are vertically connected along the z-direction, in agreement with experiment [12].

Chapter 3

Static properties of the stacked domains

3.1 Scaling analysis of the specific heat

In order to determine the phase-transition temperature and obtain the corresponding phase diagram, we compute the specific heat per lattice site defined as

$$c = \frac{1}{L^2 L_z} \frac{1}{T^2} \left(\langle H^2 \rangle - \langle H \rangle^2 \right), \tag{3.1}$$

where H is given by Eq. (2.1) and $\langle \cdots \rangle$ indicates an ensemble average. We note again that the above specific heat is calculated at constant magnetization (corresponding to constant lipid concentration in our model) of each layer. In our simulations, the ensemble average is taken by averaging over independent equilibrium spin configurations as explained in Sec. 2. For a given system size and dimensionless ratio λ, we calculate c as function of the dimensionless temperature T/J. Such a dependence of c on T/J is presented in Fig. 3.1(a) for several lateral system-sizes, L, and for $\lambda = 0.1$, $L_z = 8$, recalling that L_z is the number of layers of the 3d stack.

For each system size, we associate the peak position of the specific heat with

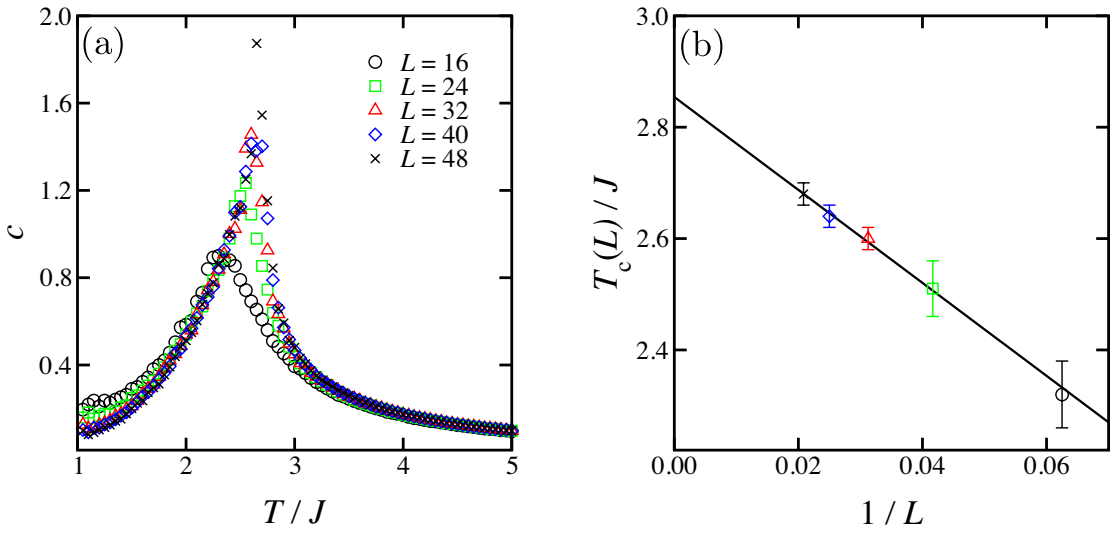

Figure 3.1: (a) Specific heat per lattice site, c, as function of the dimensionless temperature T/J, for different lateral system-size $L = 16, 24, 32, 40, 48$. The other parameters are $\overline{S}_{i,\boldsymbol{\rho}} = 0$, $\lambda = 0.1$ and $L_z = 8$. For each system size, the peak position of c is identified with an effective "phase transition" temperature. (b) Finite-size scaling analysis of the phase-transition temperature, $T_c(L)/J$ for $\lambda = 0.1$. The apparent phase-transition temperature is plotted as a function of $1/L$. The solid line is the fit given by Eq. (3.2) with $\nu = 1$ (see text). The extrapolated value for the critical temperature is $T_c(\lambda = 0.1)/J = 2.85$.

the apparent critical temperature, $T_c(L, \lambda)$, for a system with a finite size, L. Finite-size scaling analysis is then performed in order to determine the critical temperature for a slab of a finite L_z layers in the thermodynamic limit ($L \to \infty$). In Fig. 3.1(b), we plot $T_c(L, \lambda = 0.1)$ as a function of $1/L$ for the same parameters as in (a). The plotted data are fitted with the following finite-size scaling assumption:

$$T_c(L, \lambda) = T_c(\lambda) + aL^{-1/\nu}, \tag{3.2}$$

where $T_c(\lambda) = T_c(L \to \infty, \lambda)$ is the infinite system critical temperature for a given λ, a is a non-universal prefactor, and ν is the 2d critical exponent for the correlation length in the xy-plane. We set $\nu = 1$ in our analysis, following the work by Pham Phu *et al.* [24], who performed extensive MC simulations on magnetic

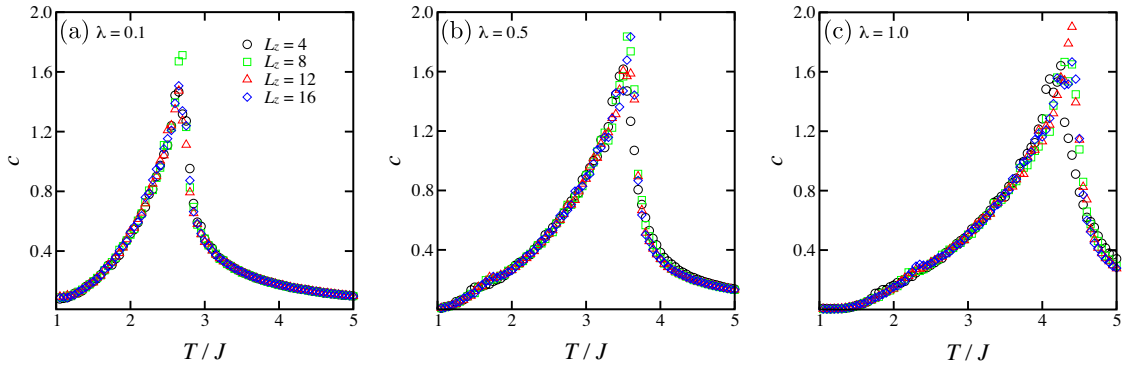

Figure 3.2: Specific heat per lattice site, c, as function of the dimensionless temperature T/J, for different systems size $L_z = 4, 8, 12, 16$ for (a) $\lambda = 0.1$, (b) $\lambda = 0.5$ and (c) $\lambda = 1$. The other parameters are $\overline{S}_{i,\rho} = 0$ and $L = 48$. The observed peak position: $T/J \approx 2.65$ in (a), 3.30 in (b) and 4.10 in (c), is almost independent of L_z, at least for $L_z \geq 8$.

Ising films (with $\lambda = 1$) [25]. We choose this 2d critical exponent for the fitting because it was shown [24] that the 2d character of the film is dominant even for $L_z = 13$. The extrapolated critical temperature for $L \to \infty$ obtained from Fig. 3.1(b) is $T_c(\lambda = 0.1)/J = 2.85$. We repeat this procedure for different values of the inter-layer interaction parameter in the range of $0 \leq \lambda \leq 1$, and determine the corresponding critical temperature, $T_c(\lambda)$. We note that the value $\nu = 1$ provides a good fitting for all the λ values examined.

Somewhat surprisingly, finite-size effects in the z-direction are much weaker as compared to those in the lateral direction. This is shown in Fig. 3.2, where we plot c as a function of T/J when (a) $\lambda = 0.1$, (b) $\lambda = 0.5$ and (c) $\lambda = 1$ for different number of layers, $L_z = 4, 8, 12, 16$, while the lateral size $L = 48$ is kept fixed. For all λ values studied here ($0.1 \leq \lambda \leq 1$), the observed peak position: $T/J \approx 2.65$ in (a), 3.30 in (b) and 4.10 in (c), is almost independent of L_z, at least for $L_z \geq 8$. This means that, in our model with a fixed imposed magnetization (A/B composition) in each layer, the correlation in the z-direction is very strong due to the cooperative behavior of domains in different layers.

For fully equilibrated configurations, as shown in Fig. 2.3 after 10^7 MCS, the

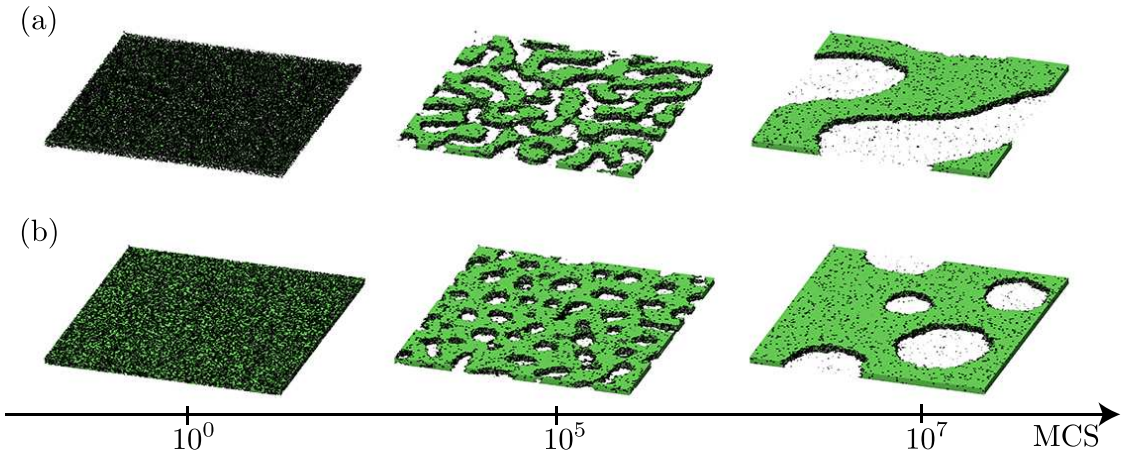

Figure 3.3: Time evolution of phase-separated domains in a stacked 2d Ising model of eight layers, $L_z = 8$, at different MC steps for (a) $\overline{S}_{i,\boldsymbol{\rho}} = 0$ and (b) $\overline{S}_{i,\boldsymbol{\rho}} = 0.4$. The other parameters are $\lambda = 0.1$, $T/J = 2.0$ and $L = 256$.

domains are highly connected vertically along the z-direction, from the bottom layer to the top one. This is also shown in Fig. 3.3 in which the columnar structure of domains in different layers is clearly shown. Hence, the correlation length in this direction exceeds L_z, and the constraint of fixed magnetization (A/B composition) in each layer induces a strong structural correlation in the z-direction even though the inter-layer interaction J' is smaller than the intra-layer interaction J ($\lambda \leq 1$). A more quantitative argument for the domain connectivity will be given later. Because the number of layers, L_z, barely affects the MC results as shown in Fig. 3.2 for $\lambda = 0.1$, 0.5 and 1, most of the simulations were done using $L_z = 8$, which is sufficiently large in our case to observe the asymptotic behavior of $L_z \to \infty$. For the anisotropic 3d Ising model without any constraint of conserved magnetization, as previously studied in Ref. [19], a very weak system-size dependence of the apparent critical temperature was observed by measuring the *planar* susceptibility.

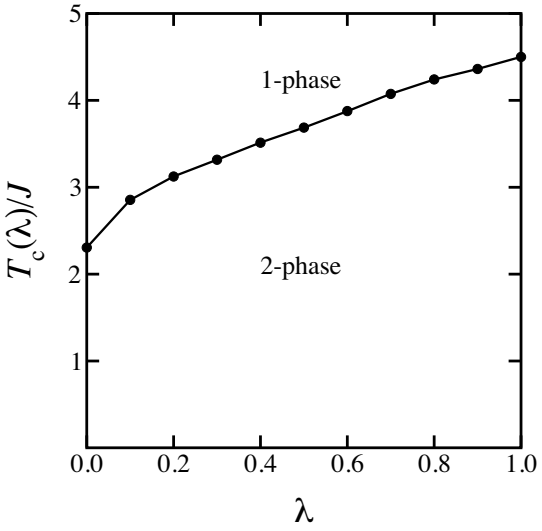

Figure 3.4: The phase-separation temperature, $T_c(\lambda)/J$, at the critical composition, as a function of the interaction parameter λ for symmetric A/B mixtures, $\overline{S}_{i,\boldsymbol{\rho}} = 0$. The system is in a phase-separated state below the solid line, and in a one-phase state above the line.

3.2 Phase diagram

The results of finite-size scaling analysis are shown in Fig. 3.4, where we plot T_c as a function of λ. The critical temperature interpolates between the 2d and 3d Ising results, $T_c^{2d} < T_c(\lambda) < T_c^{3d}$; the exact value in 2d (corresponding to $\lambda = 0$) is known to be $T_c^{2d}/J = 2/\ln(1+\sqrt{2}) \approx 2.269$ for square lattices [26], and the numerical estimate in 3d (corresponding to $\lambda = 1$) is $T_c^{3d}/J \approx 4.511$ for cubic lattices [27]. These two limits are recovered in our simulations and are seen in Fig. 3.4 for $\lambda = 0$ and 1, respectively. Although a more detailed λ-dependent scaling behavior of $T_c(\lambda)$ was previously discussed in the limit of very small λ [19, 28], we shall generalize the argument for the anisotropic case of finite λ, $0 \leq \lambda \leq 1$. When $T < T_c(\lambda)$, the stack undergoes a phase separation, and the inplane domains rich in lipid A (spin up) are interconnected along the z-direction, bridging between adjacent layers and forming large connected domains of the same average composition. The same feature also occurs for the B-rich domains. Such

a behavior can be clearly observed in Fig. 3.3.

3.3 Connectivity of domains

In order to monitor quantitatively the degree of inter-connectivity of domains in different layers, we define the following quantity:

$$\delta^2 = \frac{1}{L^2} \left\langle \sum_{\boldsymbol{\rho}} \left(\frac{1}{L_z} \sum_i S_{i,\boldsymbol{\rho}} - \overline{S}_{i,\boldsymbol{\rho}} \right)^2 \right\rangle , \tag{3.3}$$

where the average is taken over equilibrated MC configurations as explained above. This quantity can be cast also as:

$$\delta^2 = \frac{1}{L^2 L_z^2} \sum_{\boldsymbol{\rho}} \sum_{i,j} \left\langle (S_{i,\boldsymbol{\rho}} - \overline{S}_{i,\boldsymbol{\rho}})(S_{j,\boldsymbol{\rho}} - \overline{S}_{j,\boldsymbol{\rho}}) \right\rangle , \tag{3.4}$$

and represents a special "magnetic susceptibility", where the correlations are taken only along the z-direction and then averaged laterally in each of the planes. When the domains are connected along the z-direction, the summation over different i-layers will produce a large value of δ, while δ is small if the domains are uncorrelated across the layers even for $T < T_c(\lambda)$. In Fig. 3.5, we plot δ^2 as a function of T/J for different values of λ, while fixing $L = 16$ and $L_z = 8$. Notice that even for λ as small as 0.05 (blue diamonds), δ^2 tends to increase as the temperature decreases below $T_c(\lambda)$. This means that the domains are connected in the z-direction once the phase separation takes place. On the other hand, domains are independent and uncorrelated only when the inter-layer interaction is extremely small, i.e, $\lambda \leq 0.001$ in Fig. 3.5. The situation is found to be marginal when $\lambda = 0.01$ (red triangles) because δ^2 then slightly deviates from zero at low temperatures.

Based on our MC results, we conclude that in the thermodynamic limit, $L \to \infty$, domains will always be connected for any finite inter-layer interaction, $J' > 0$. We give now a simple argument supporting this conclusion, and show that in the limit $L \to \infty$ but with a finite number of layers, L_z, the domains in different layers

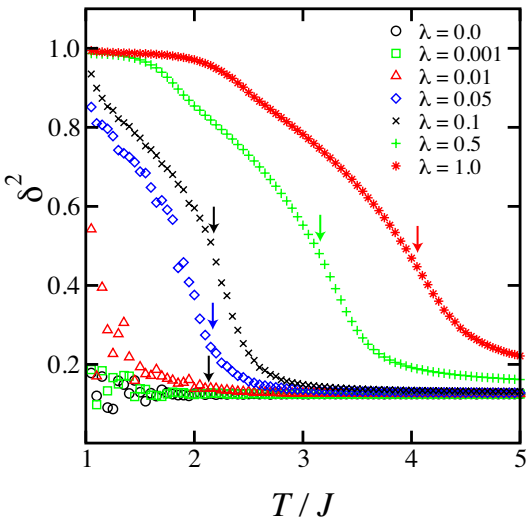

Figure 3.5: The out-of-plane domain connectivity, δ^2, defined in Eq. (3.3), as a function of the dimensionless temperature T/J, for different values of $\lambda = 0$, 0.001, 0.01, 0.05, 0.1, 0.5, 1.0. The other parameters are $\overline{S}_{i,\boldsymbol{\rho}} = 0$, $L = 16$ and $L_z = 8$. The transition temperatures for different λ values are indicated by arrows. The value of δ^2 becomes larger when domains are correlated along the z-direction between different layers. This increase in δ^2 is observed for lower temperatures and larger λ.

are uncorrelated only when $J' = 0$ ($\lambda = 0$) is strictly obeyed. For the symmetric A/B case ($\overline{S}_{i,\boldsymbol{\rho}} = 0$), each layer will eventually phase separate into two semi-infinite domains: one composed by the A lipid (spin up) and the other by the B lipid (spin down), as shown schematically in Fig. 3.6. When the domains are fully correlated in the z-direction, as in Fig. 3.6(a), the total free energy of the stack consists of the contributions:

$$F_{\rm con} = -J' L_z L^2 + F_{\rm intra}, \tag{3.5}$$

where $F_{\rm intra}$ accounts for the intra-layer interactions. On the other hand, when the inplane domains are completely random and disconnected, as sketched in Fig. 3.6(b), the total free energy is dominated by an entropy contribution of arranging a random stack of A and B domains along the z-direction,

$$F_{\rm dis} = -T L_z \ln 2 + F_{\rm intra}, \tag{3.6}$$

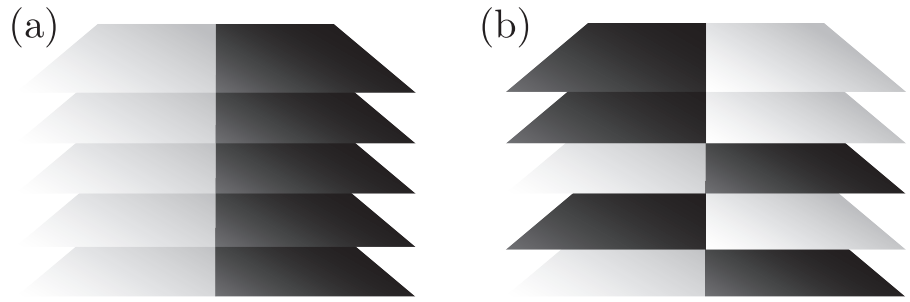

Figure 3.6: Schematic representation of phase separated domains in a stack of membranes. Black and white domains are rich in A and B lipids, respectively. Two extreme cases are shown; (a) domains are fully connected in the z-direction, (b) domains are arranged at random and are disconnected.

with the same F_{intra} as before because this term is common for both free energies. By comparing Eqs. (3.5) and (3.6), the threshold inter-layer interaction, $(J')^*$, separating the two states, is given by:

$$(J')^* = \frac{T \ln 2}{L^2}. \tag{3.7}$$

Notice that $(J')^*$ depends on L but not on L_z. For finite temperatures, it vanishes in the thermodynamic limit of $L \to \infty$. Hence, this simple scaling argument suggests that domains are always connected in the z-direction for any finite value of J'. Therefore, for all $\lambda > 0$, in the phase-separated region (below the critical temperature) presented in Fig. 3.4, domains should always form interconnected structures along the z-direction. As shown in Eqs. (3.5) and (3.6), the internal energy scales with L^2, while the entropy due to the random stacking of domains does not depend on L. Hence, the entropic effect can never overcome the internal energy in the thermodynamic limit, and leads to the stability of the columnar structure. This conclusion is not in agreement to that of Tayebi *et al.* [14], who claimed that there is a "multi-phase" state in which domains are not aligned and have different compositions even in thermodynamical equilibrium.

In the simulations, $(J')^*$ can be finite due to finite-size effects. For instance, if the temperature is chosen to be $T/J = 1$ in Fig. 3.5, the threshold value for $L = 16$

can be estimated as $\lambda^* = (J')^*/J \approx 2.7 \times 10^{-3}$. Since $\lambda = 10^{-2}$ (red triangles in Fig. 3.5) exceeds this threshold, the corresponding δ^2 takes larger values at low temperatures. Moreover, the very weak finite-size effects along the z-direction is consistent with the lack of L_z-dependence of $(J')^*$ in Eq. (3.7).

Chapter 4

Dynamics of phase separation

4.1 Interface length as a function of time

We address now the effects of inter-layer interaction on the dynamics of phase separation as the system converges towards its thermal equilibrium state. Under the assumption that scaling laws can be applied, the average domain size R increases according to a temporal power-law: $R(t) \sim t^{\alpha}$ [11]. For 2d systems for which the total domain area is conserved, the average domain size R is inversely proportional to the total interface length ℓ, i.e., $R \sim \ell^{-1}$ [29, 30]. This can easily be seen because R and ℓ are related by $\ell = 2\pi nR \sim nR$, where n is the number of domains, and the total area of all domains, $A = \pi nR^2 \sim nR^2$, is a conserved quantity. Hence, within the scaling hypothesis, the total interface length (in 2d) should behave as

$$\ell(t) \sim t^{-\alpha}. \tag{4.1}$$

In our stacked Ising model, we calculate the interface length in each of the layers and average it over different layers. Note that the total interface length is proportional to the first term of the Hamiltonian in Eq. (2.1), which enumerates the number of bonds across the inplane A/B interface.

4.2 Constant temperature

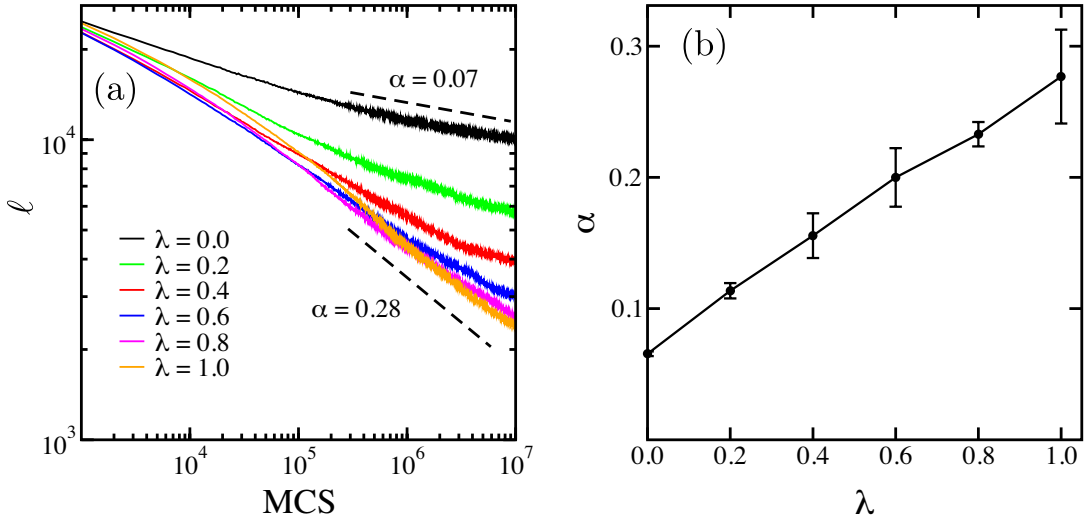

Figure 4.1: (a) The temporal evolution of the total interface length ℓ as a function of time (MCS) for different values of $\lambda = 0$, 0.2, 0.4, 0.6, 0.8, 1.0, and for a temperature quench from the one-phase state ($T \to \infty$) into the two-phase state at $T/J = 2.0$. The A/B mixture is symmetric, $\overline{S}_{i,\rho} = 0$, $L = 256$ and $L_z = 8$. The average over three independent MC runs is taken for each λ value. The two dashed lines represent a power-law behavior with exponent $\alpha = 0.07$ and 0.28, which roughly bound the two limiting behaviors of the λ-dependent exponent, α. (b) The domain growth exponent α as a function of λ, as obtained from (a).

In Fig. 4.1(a), we plot the temporal evolution of the total interface length in 2d, $\ell(t)$, (and averaged along the z-direction), as a function of time measured in MC steps. The temperature quench into the two-phase region is done for a fixed temperature, $T/J = 2.0 < T_c(\lambda)$, in order to mimic the experiment that is conducted at fixed room temperature. Several values of λ are studied, and the other parameters are $L = 256$ and $L_z = 8$, with averages taken over three independent MC runs. For each λ value, the scaling behavior of Eq. (4.1) is analyzed, and we extract the growth exponent α from the late stage kinetics. We find that for $\lambda = 0$ (2d case), the growth exponent has the smallest value of $\alpha \approx 0.07$, while for $\lambda > 0$, it is a function of λ and increases up to $\alpha \approx 0.28$, as

shown in Fig. 4.1(b).

Although this result may explain the fact that the phase separation has an accelerated dynamics in stacked membranes as compared to GUVs (isolated single membranes), we should keep in mind that $T_c(\lambda)$ increases as function of the inter-layer coupling $\lambda > 0$, as shown in Fig. 3.4. As long as the final quench temperature is fixed to $T/J = 2.0$, the temperature quench depth defined by $\Delta T = T_c(\lambda) - T$ becomes larger as the value of λ is increased. This may explain why the growth exponent α becomes larger with increasing λ, for a fixed T-quench.

4.3 Constant quench ratio

In order to have a better comparison between different λ values, we evaluate in Fig. 4.2 the growth exponent in a different way. We now keep a constant quench ratio $T/T_c(\lambda) = 0.6$, where T is the final quench temperature, and the critical temperature $T_c(\lambda)$ depends on λ, as shown in Fig. 3.4. For these deeper temperature quenches (farther from $T_c(\lambda)$), the estimated growth exponent is $\alpha \approx 0.24$ for $\lambda = 0$ (pure 2d case), and $0.13 \leq \alpha \leq 0.16$ for $0.2 \leq \lambda \leq 1.0$. Note that the α-values are only weakly dependent on $\lambda > 0$.

Finally, we elaborate on the decreasing λ-dependence of the growth exponent α, and show that this behavior is consistent with the change in the dimensionality of the stack from 2d to 3d. In general, the growth exponent associated with phase separation depends on the dimensionality [31]. In this context, we mention the scaling argument of Binder and Stauffer on phase-separation dynamics of particles that undergo cluster reaction and diffusion processes [32, 33, 34, 35]. Under the assumption that most particles that leave a cluster reimpinge on the same cluster at later times, the diffusion coefficient D of a cluster of size R was shown to scale as $D \sim R^{-(1+d)}$, where d is the embedded space dimension. If we further assume that the domain size R is the only length scale in the system, the scaling relation for a simple diffusion process is given by $R^2 \sim Dt$. This argument yields the growth exponent to be $\alpha = 1/(3 + d)$. Hence, the predicted values from this

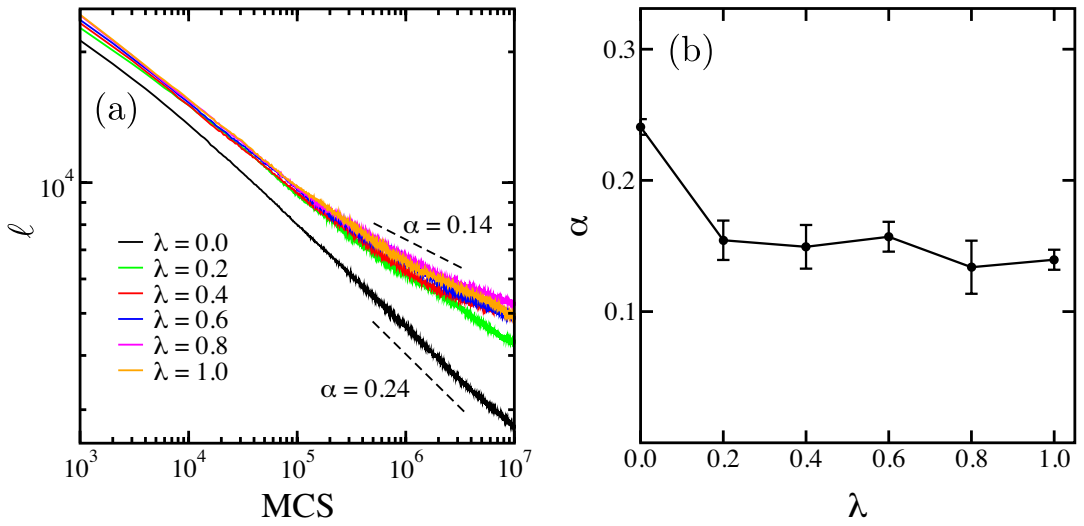

Figure 4.2: The temporal evolution of the total interface length ℓ as a function of time (MCS) for different values of $\lambda = 0$, 0.2, 0.4, 0.6, 0.8, 1.0, and for a temperature quench from the one-phase state into the two-phase one, with final temperature satisfying $T = 0.6T_c(\lambda)$. The A/B mixture is symmetric, $\overline{S}_{i,\boldsymbol{\rho}} = 0$, $L = 256$ and $L_z = 8$. The average over three independent MC runs is taken for each λ value. The two dashed lines represent a power-law behavior with exponents $\alpha = 0.14$ and $\alpha = 0.24$. (b) The domain growth exponent α as a function of λ, as obtained from (a).

scaling conjecture are $\alpha = 1/5$ for $d = 2$ and $\alpha = 1/6$ for $d = 3$.

Our simulation results, namely, $\alpha \approx 0.24$ for $\lambda = 0$ and $\alpha \approx 0.14$ for $\lambda \geq 0.2$ compare favorably with this prediction. The growth exponent decreases for finite λ because the system crosses-over from 2d to 3d. This is due to the fact that the growing phase-separated domains are inter-connected along the z-direction for $\lambda > 0$. It should be noted, however, that the absolute value of α obtained from the simulation is not universal but strongly depends on the quench depth as shown in Fig. 4.1. This explains why the above exponents are not in complete agreement with the simple scaling argument of Binder and Stauffer.

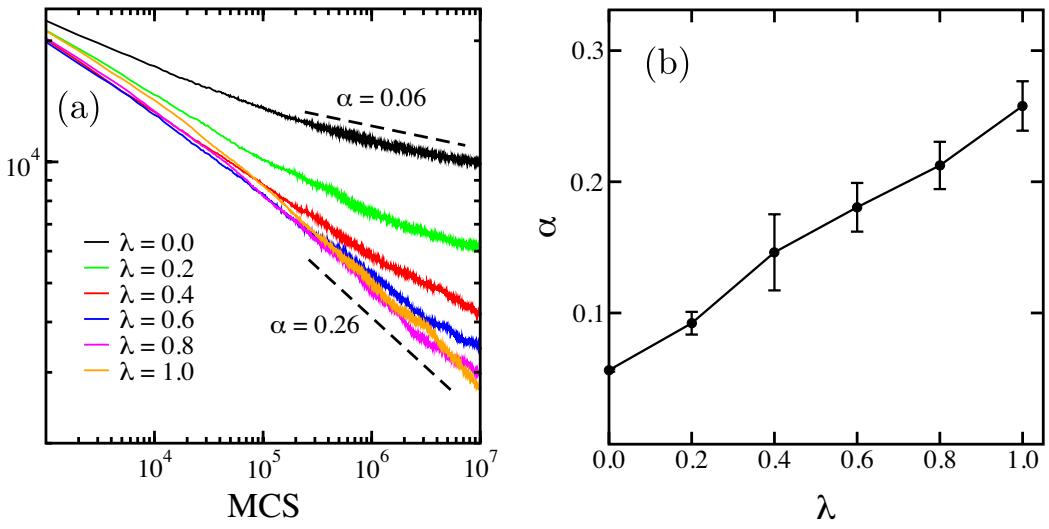

Figure 4.3: (a) The temporal evolution of the total interface length ℓ as a function of time (MCS) for different values of $\lambda = 0$, 0.2, 0.4, 0.6, 0.8, 1.0, and for a temperature quench from the one-phase state ($T \to \infty$) into the two-phase state at $T/J = 2.0$. The A/B mixture is asymmetric, $\overline{S}_{i,\boldsymbol{\rho}} = 0.4$, $L = 256$ and $L_z = 8$. The average over three independent MC runs is taken for each λ value. The two dashed lines represent a power-law behavior with exponent $\alpha = 0.06$ and 0.26, which roughly bound the two limiting behaviors of the λ-dependent exponent, α. (b) The domain growth exponent α as a function of λ, as obtained from (a).

4.4 Off-critical compositions

We have discussed the case of $\overline{S}_{i,\boldsymbol{\rho}} = 0$ corresponding to the critical composition of the A/B lipid mixture. Now we investigate the dynamics of phase separation for off-critical compositions $\overline{S}_{i,\boldsymbol{\rho}} \neq 0$ such as shown in Fig. 3.3(b). In Fig. 4.3, we plot the temporal evolution of the total interface length in 2d, $\ell(t)$, as a function of time measured in MC steps for a fixed temperature. The measurement is performed for $\overline{S}_{i,\boldsymbol{\rho}} = 0.4$ where the composition of A/B mixture is off-critical. The other parameters are $T/J = 2.0$, $L = 256$, $L_z = 8$. We find that the domain growth exponents are slightly smaller as compared with the critical case.

In Fig. 4.4, we plot the temporal evolution of $\ell(t)$ as a function of time measured in MC steps for a constant quench ratio. We keep a constant quench ratio $T/T_c =$

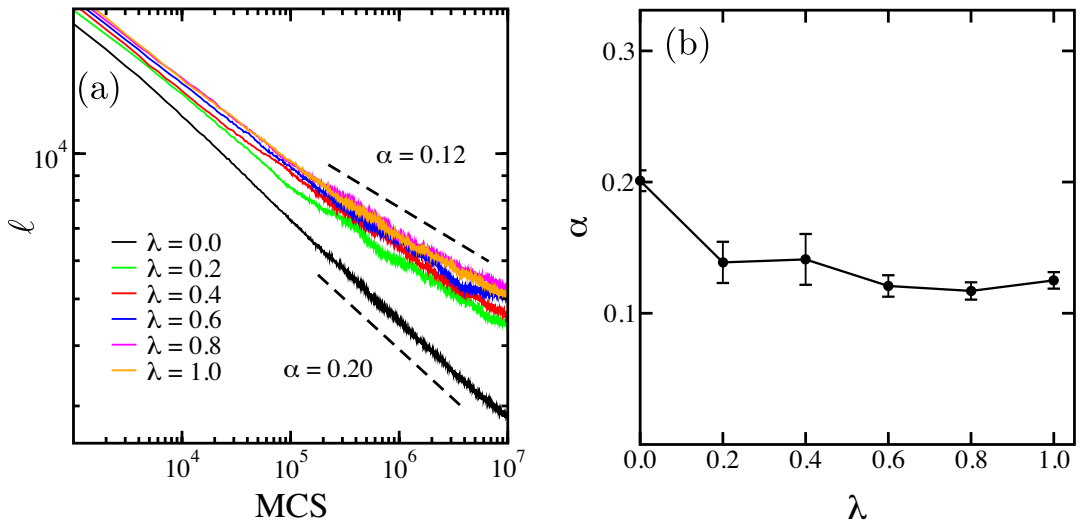

Figure 4.4: The temporal evolution of the total interface length ℓ as a function of time (MCS) for different values of $\lambda = 0$, 0.2, 0.4, 0.6, 0.8, 1.0, and for a temperature quench from the one-phase state into the two-phase one, with final temperature satisfying $T = 0.6T_c(\lambda)$. The A/B mixture is asymmetric, $\overline{S}_{i,\boldsymbol{\rho}} = 0.4$, $L = 256$ and $L_z = 8$. The average over three independent MC runs is taken for each λ value. The two dashed lines represent a power-law behavior with exponents $\alpha = 0.12$ and $\alpha = 0.20$. (b) The domain growth exponent α as a function of λ, as obtained from (a).

0.6, where the value of T_c is that of critical compositions. This is because we have not determined the phase-separation temperature yet. However, it was reported that the critical temperature is almost constant for the three-dimensional Ising model even if $\overline{S}_{i,\boldsymbol{\rho}} = 0.6$ (A/B composition = 20/80) [38]. From this result, we consider that the phase-separation temperature for $\overline{S}_{i,\boldsymbol{\rho}} = 0.4$ is almost equal to the critical case.

Both results indicate that the off-critical dynamics obeys a mechanism similar to the critical composition case. In addition, the absolute values of domain growth exponents in off-critical case is relatively small as shown in Fig. 4.5. The difference of the power-law between the critical and the off-critical cases is about 0.02. We conjecture that this is because the domain shape is different between these two cases as shown in Fig. 3.3. Otherwise the phase separation temperature for $\overline{S}_{i,\boldsymbol{\rho}} =$

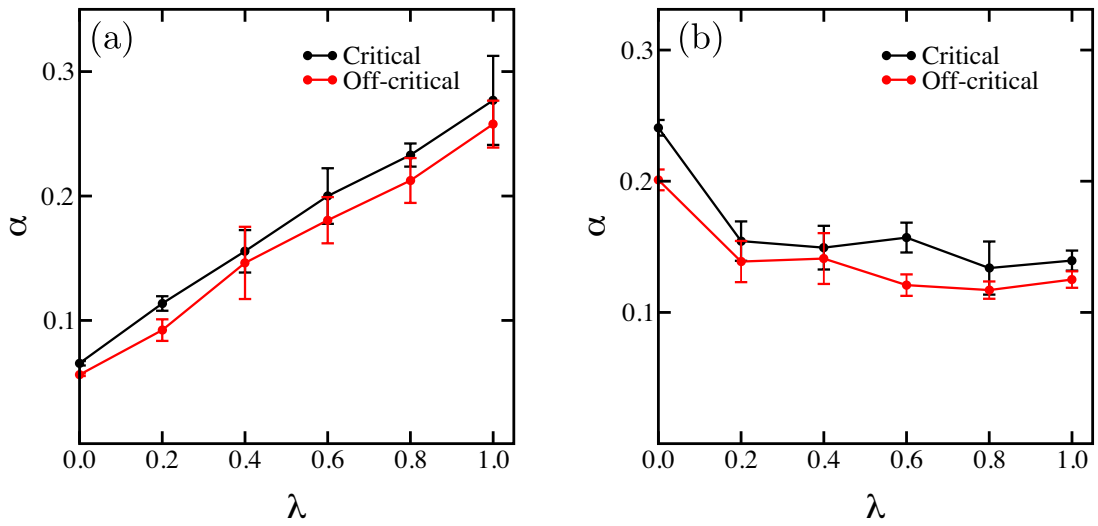

Figure 4.5: The domain growth exponent α as a function of λ. the critical case ($\overline{S}_{i,\boldsymbol{\rho}} = 0.0$) and the off-critical case ($\overline{S}_{i,\boldsymbol{\rho}} = 0.4$) are compared in these graphs. The other parameters are $L = 256$ and $L_z = 8$. (a) The temperature quench is done for $T/J = 2.0$. (b) The temperature quench is done with keeping a consant quench ratio $T/T_{\rm c}(\lambda) = 0.6$.

0.4 is slightly lower than for $\overline{S}_{i,\boldsymbol{\rho}} = 0$.

Chapter 5

Concluding remarks

Motivated by recent works of Tayebi *et al.* [12, 14], who studied experimentally and theoretically the phase separation in stacks of multi-component lipid bilayers, we have investigated the stacked 2d Ising model given in Eq. (2.1). We use a Monte Carlo simulation scheme with Kawasaki exchange dynamics that conserves the order parameter in each layer, in order to investigate both equilibrium and dynamical features. Performing finite-size scaling analysis only in the lateral direction, while keeping the stack thickness fixed (mimicking the experiment), we determine the phase-transition temperature, $T_c(\lambda)$, by changing the inter-layer interaction parameter $\lambda = J'/J$. As shown in Fig. 3.4, the phase-transition temperature interpolates between that of the 2d and 3d Ising model.

One of our main conclusions is that domains in each one of the layers are always interconnected along the z-direction, forming a continuous columnar structure for any finite inter-layer interaction $J' > 0$, as shown in Fig. 3.3. This domain structure is in accord with the experimental findings for stacks of few dozen to few hundred layers [12]. However, the "multi-phase" region in which there are unaligned inplane domains with different composition, as was predicted in Ref. [14], is not found in our study at thermal equilibrium. Of course that such a "multi-phase" state can be transiently observed before the system reaches its fully equilibrated state, as can be observed in Figs. 2.3 and 3.3.

We have also investigated the temporal evolution of domain formation in the stacked 2d Ising model. When the inter-layer interaction λ increases, the phase separation appears to have an accelerated dynamics as can be seen by the larger values of the growth exponent, α, shown in Fig. 4.1(b). However, these larger α values are mainly due to an increase in the phase-transition temperature, $T_{\rm c}(\lambda)$, as function of λ; thus, a larger effective temperature quench, $\Delta T = T_{\rm c}(\lambda) - T$, for fixed T. When the final temperature quench T is fixed relative to the phase-transition temperature as shown in Fig. 4.2 for $T = 0.6T_{\rm c}(\lambda)$, the growth exponent even decreases as the λ value is increased. Our numerical findings for the growth exponent α are different than the value of $\alpha \approx 0.455$, as found in the experiment [12]. One possible explanation for this discrepancy can be the lack of hydrodynamic interactions in our MC simulations [13].

In this work, we have mainly discussed the case of $\overline{S}_{i,\boldsymbol{\rho}} = 0$, corresponding to the critical composition of the A/B lipid mixture. Currently, we are investigating the dynamics of phase separation for off-critical compositions, $\overline{S}_{i,\boldsymbol{\rho}} \neq 0$ [see Fig. 3.3(b)]. For such compositions, the phase-transition temperature is smaller than the critical temperature. In the present simulations, the average A/B lipid composition (order parameter of the Ising model) in each bilayer is restricted to stay the same. In the future, we plan to study membrane stacks where each layer has a different but fixed composition [36]. Furthermore, since it is known from simulations that the presence of a supporting solid substrate affects the dynamics of membrane domain growth [37], it will be of interest to incorporate this substrate effect in future studies.

Appendix A

Finite-size scaling analysis

10^6 MCS for equilibrium are performed and 10^5 independent samples are averaged in each temperature with annealing. The peak of specific heat in each size is taken as a function of $1/L$ for finite size-staling. Fitting by gnuplot are done as ν is parameter and is equal to 1, respectively.

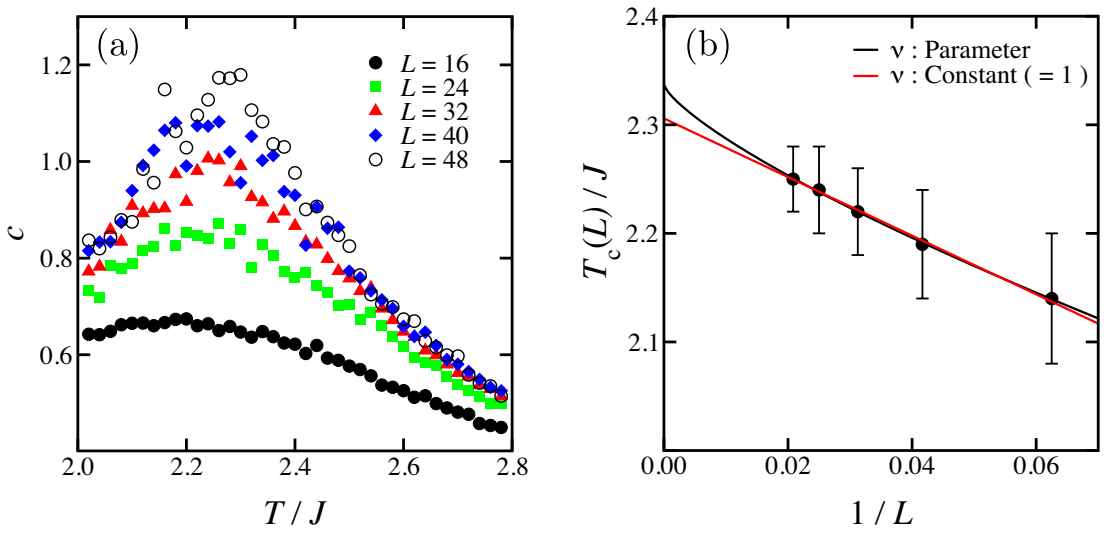

Figure A.1: (a) Specific heat for $\lambda = 0.0$, (b) Finite-size scaling for $\lambda = 0.0$.

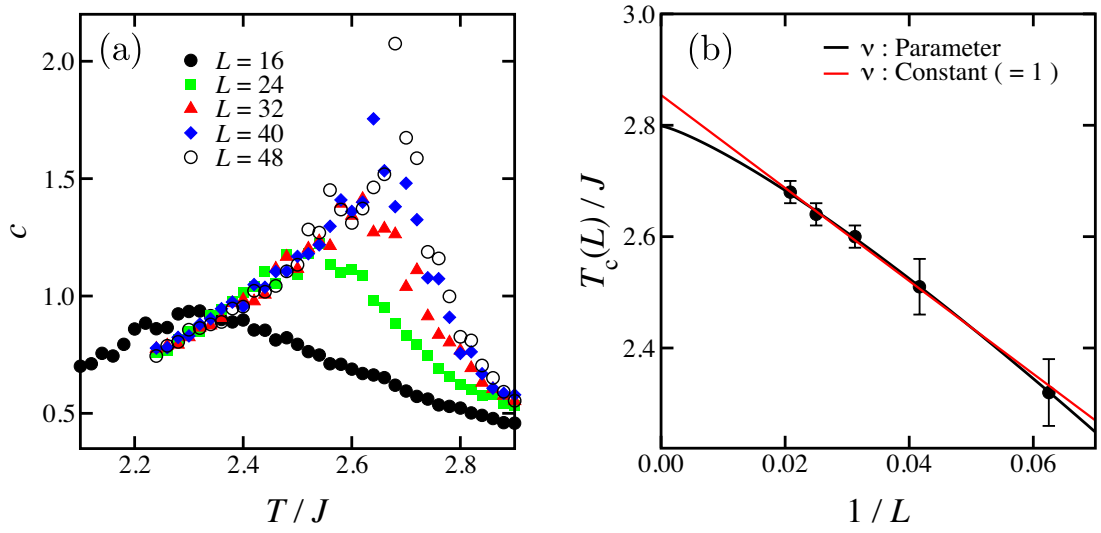

Figure A.2: (a) Specific heat for $\lambda = 0.1$, (b) Finite-size scaling for $\lambda = 0.1$.

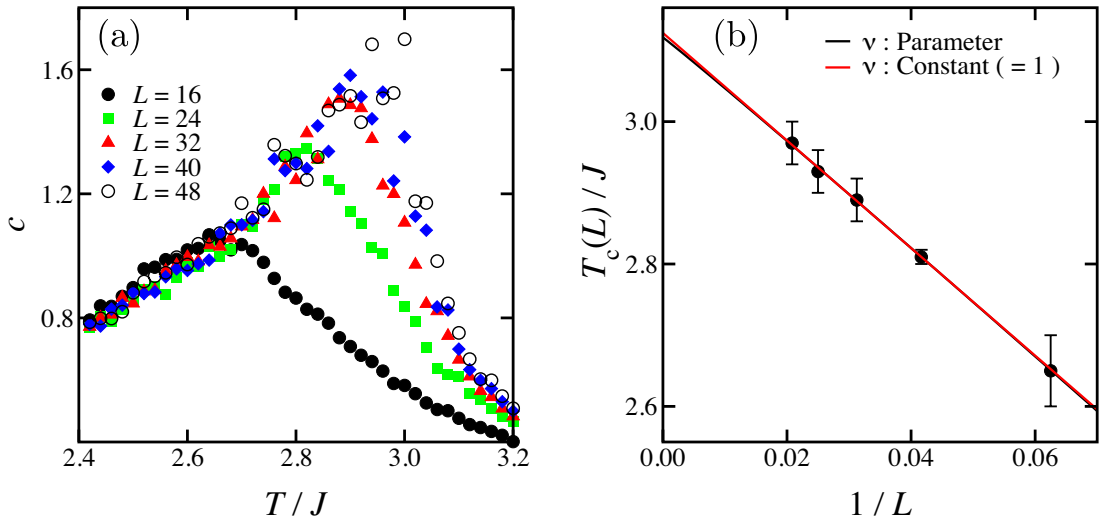

Figure A.3: (a) Specific heat for $\lambda = 0.2$, (b) Finite-size scaling for $\lambda = 0.2$.

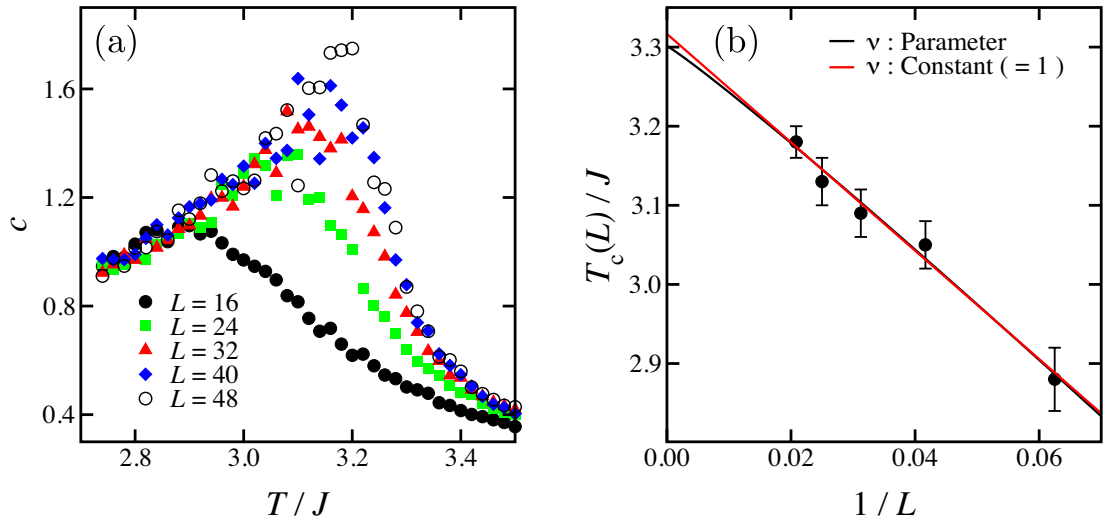

Figure A.4: (a) Specific heat for $\lambda = 0.3$, (b) Finite-size scaling for $\lambda = 0.3$.

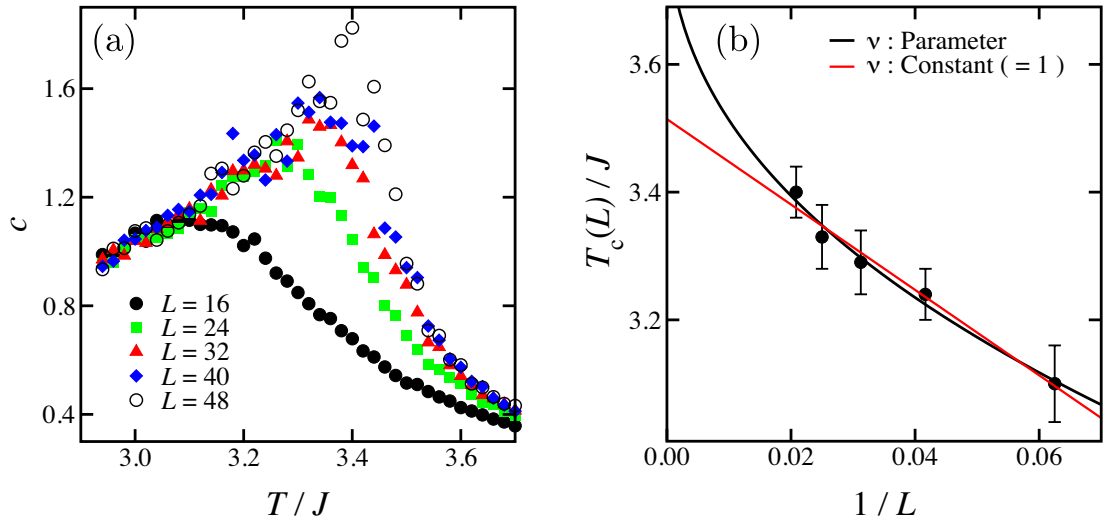

Figure A.5: (a) Specific heat for $\lambda = 0.4$, (b) Finite-size scaling for $\lambda = 0.4$.

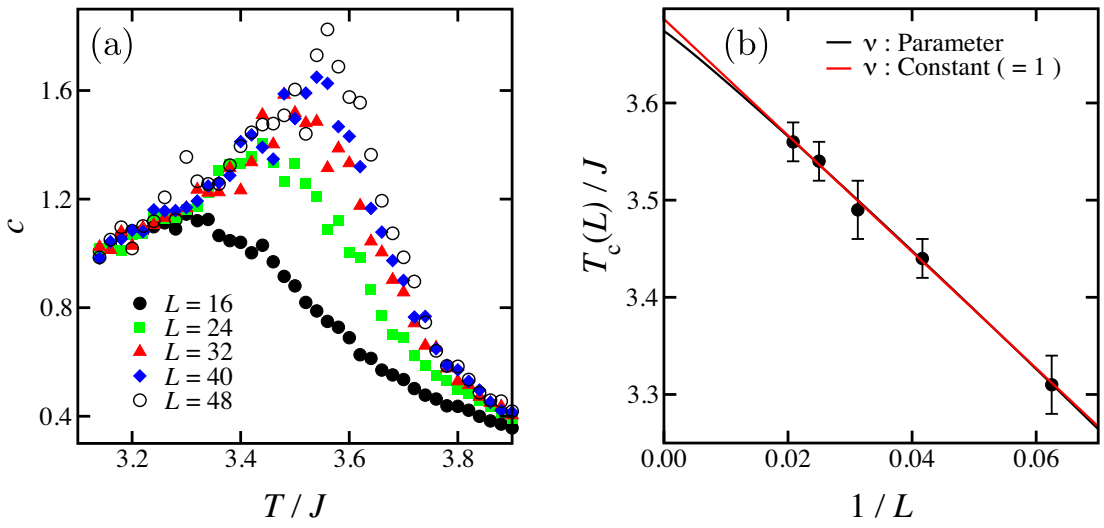

Figure A.6: (a) Specific heat for $\lambda = 0.5$, (b) Finite-size scaling for $\lambda = 0.5$.

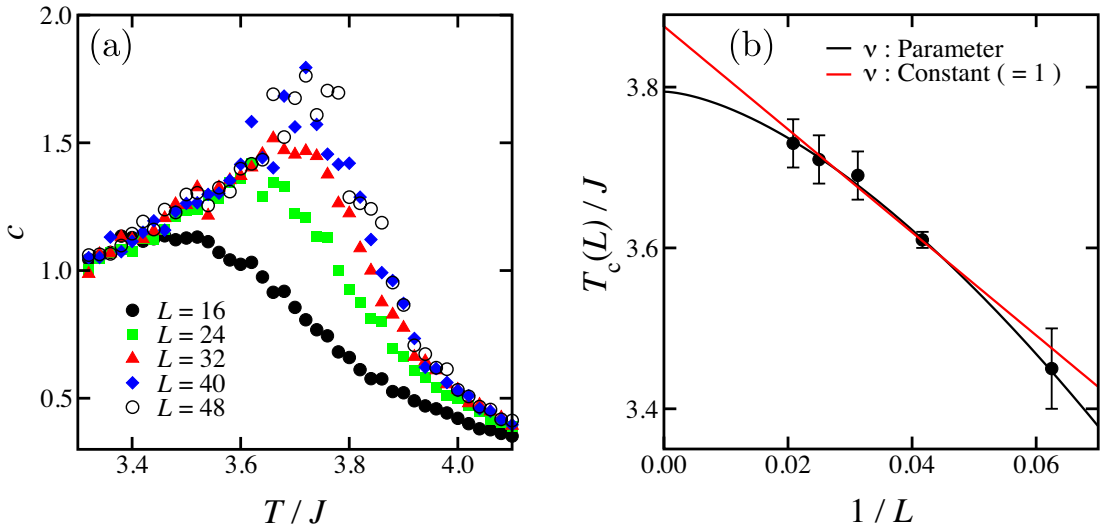

Figure A.7: (a) Specific heat for $\lambda = 0.6$, (b) Finite-size scaling for $\lambda = 0.6$.

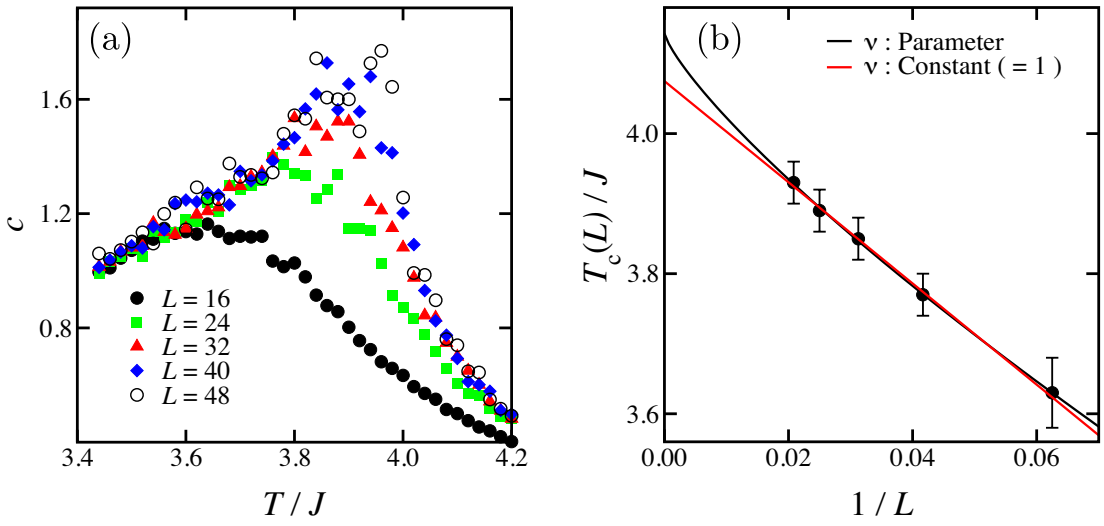

Figure A.8: (a) Specific heat for $\lambda = 0.7$, (b) Finite-size scaling for $\lambda = 0.7$.

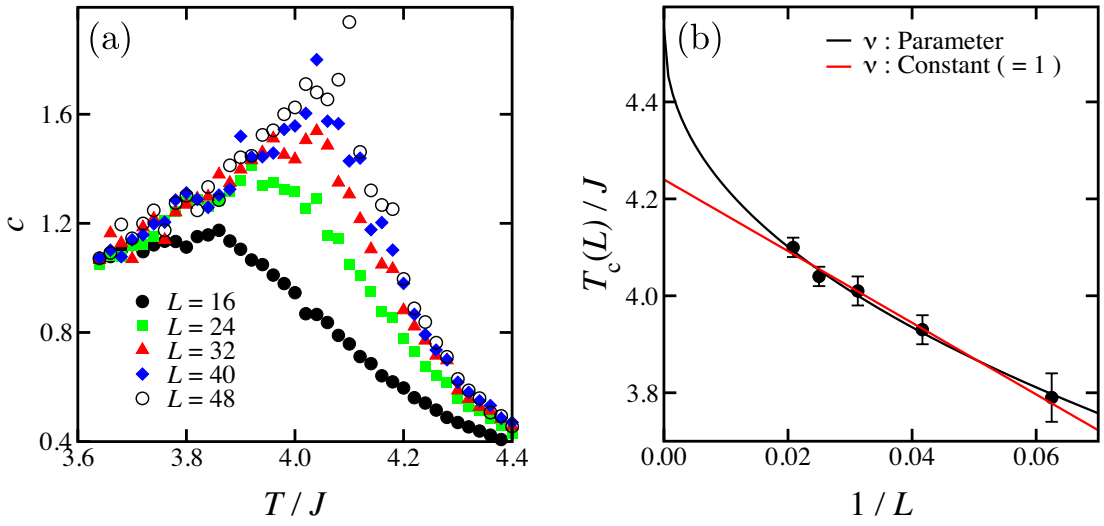

Figure A.9: (a) Specific heat for $\lambda = 0.8$, (b) Finite-size scaling for $\lambda = 0.8$.

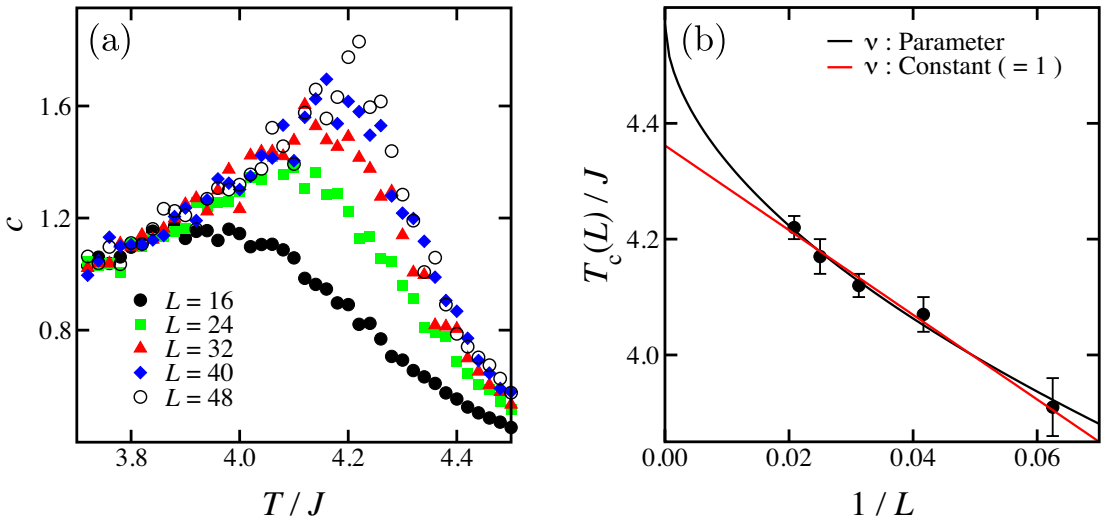

Figure A.10: (a) Specific heat for $\lambda = 0.9$, (b) Finite-size scaling for $\lambda = 0.9$.

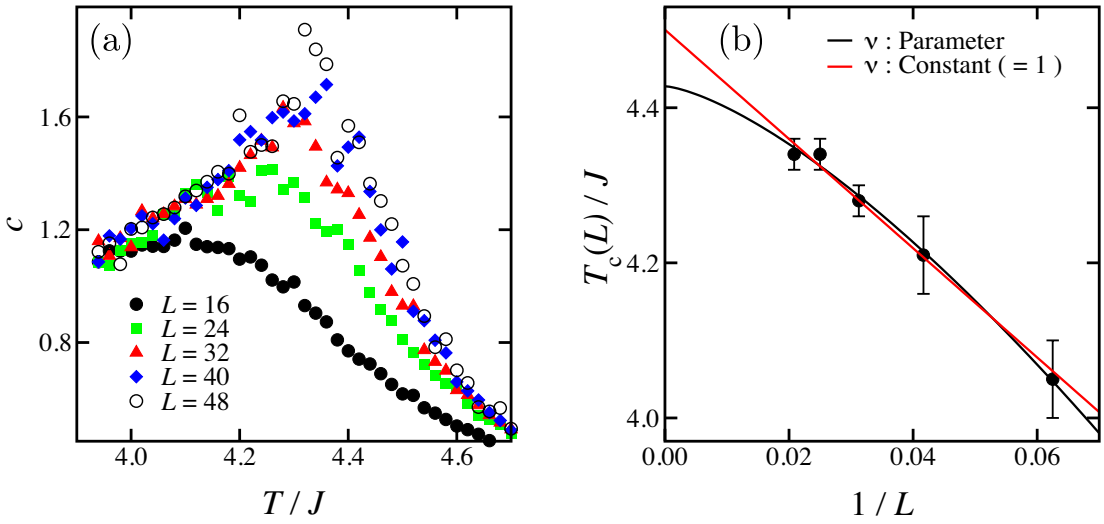

Figure A.11: (a) Specific heat for $\lambda = 1.0$, (b) Finite-size scaling for $\lambda = 1.0$.

Appendix B

Phase diagrams for $L_z = 4$ and 8

From the finite-size scaling analysis, we obtain the critical temperature for each λ. This graph is a phase diagram. By comparing the data between $L_z = 4$ and 8, it is found that T_c is close to the value of 3D Ising at $\lambda = 1.0$.

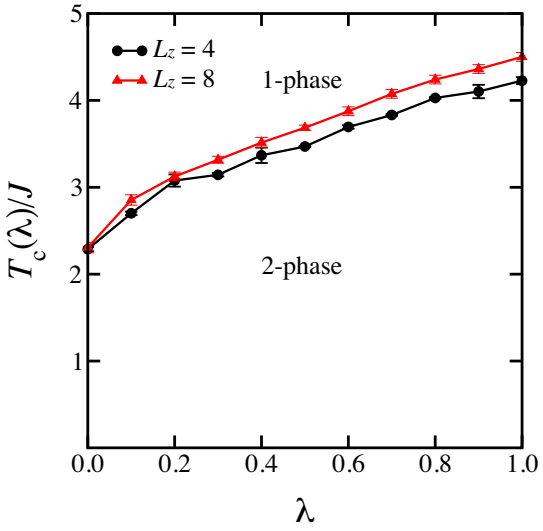

Figure B.1: Phase diagram

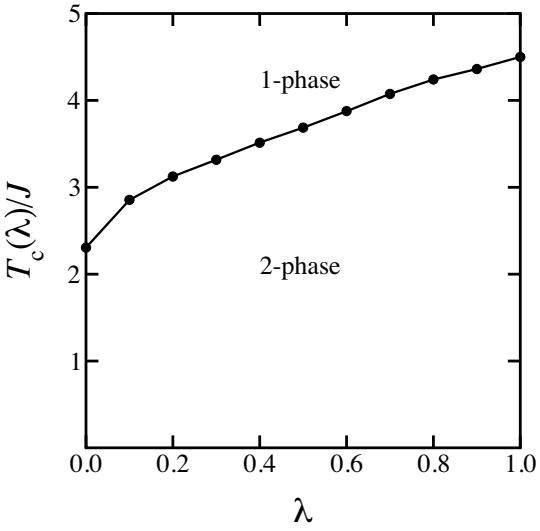

Figure B.2: Phase diagram for $\nu = 1$

Table B.1: Difference of critical temperature between $L_z = 4$ and $L_z = 8$

λ	$T_c(L_z = 4)$	$T_c(L_z = 8)$
0.0	2.287964	2.3059
0.1	2.713289	2.85417
0.2	3.0763	3.1245
0.3	3.149456	3.3166
0.4	3.36851	3.51432
0.5	3.475642	3.6863
0.6	3.691266	3.8755
0.7	3.831555	4.075
0.8	4.028575	4.24
0.9	4.102438	4.3617
1.0	4.227895	4.5006

Appendix C

Metropolis algorithm

In this Appendix, the source code of Metropolis algorithm is shown. A Boltzmann probability is calculated in the other subroutine in order to reduce the calculation cost.

Listing C.1: Source code of Metropolis algorithm

```
1   subroutine Metropolis
2     implicit none
3     integer ispin,x1,x2,y1,y2
4     integer neutral1,left,right,up,down
5     integer neutral2,hidari,miggie,ue,shita
6     integer z,above1,above2,below1,below2
7     integer Vspin,intra,inter
8       do ispin=1,N
9          !RANDOM XYZ POSITIONS ARE CHOSEN
10         x1=int(L*rnd(0))+1
11         y1=int(L*rnd(0))+1
12         z=int(Lz*rnd(0))+1
13         !SELECT A NEAREST NEIGHBOUR SPIN
14         if(rnd(0).lt.0.5) then
15            if(rnd(0).lt.0.5) then
16               x2=x1+1; y2=y1
```

```
17              else
18                 x2=x1-1; y2=y1
19              end if
20           else
21              if(rnd(0).lt.0.5) then
22                 x2=x1; y2=y1+1
23              else
24                 x2=x1; y2=y1-1
25              end if
26           end if
27           !PERIODIC B.C
28           if(x2.eq.L+1) then
29              x2=1
30           else if(x2.eq.0) then
31              x2=L
32           end if
33           if(y2.eq.L+1) then
34              y2=1
35           else if(y2.eq.0) then
36              y2=L
37           end if
38           neutral1=spin(x1,y1,z); neutral2=spin(x2,y2,z)
39           !IF neutral1==neutral2, GO TO NEXT DO-LOOP
40           if (neutral1.ne.neutral2) then
41              if (x1.eq.1) then
42                 left=spin(L,y1,z); right=spin(2,y1,z)
43              else if (x1.eq.L) then
44                 left=spin(L-1,y1,z); right=spin(1,y1,z)
45              else
46                 left=spin(x1-1,y1,z); right=spin(x1+1,y1,z)
47              end if
48              if (y1.eq.1) then
```

```
49                up=spin(x1,2,z); down=spin(x1,L,z)
50             else if (y1.eq.L) then
51                up=spin(x1,1,z); down=spin(x1,L-1,z)
52             else
53                up=spin(x1,y1+1,z); down=spin(x1,y1-1,z)
54             end if
55             if(x2.eq.1) then
56                hidari=spin(L,y2,z); miggie=spin(2,y2,z)
57             else if(x2.eq.L) then
58                hidari=spin(L-1,y2,z); miggie=spin(1,y2,z)
59             else
60                hidari=spin(x2-1,y2,z); miggie=spin(x2+1,y2,z
                     )
61             end if
62             if(y2.eq.1) then
63                ue=spin(x2,2,z); shita=spin(x2,L,z)
64             else if(y2.eq.L) then
65                ue=spin(x2,1,z); shita=spin(x2,L-1,z)
66             else
67                ue=spin(x2,y2+1,z); shita=spin(x2,y2-1,z)
68             end if
69             if (z.eq.1) then
70                above1=spin(x1,y1,2); above2=spin(x2,y2,2)
71                below1=spin(x1,y1,Lz); below2=spin(x2,y2,Lz)
72             else if (z.eq.Lz) then
73                above1=spin(x1,y1,1); above2=spin(x2,y2,1)
74                below1=spin(x1,y1,Lz-1); below2=spin(x2,y2,Lz
                     -1)
75             else
76                above1=spin(x1,y1,z+1); above2=spin(x2,y2,z
                     +1)
77                below1=spin(x1,y1,z-1); below2=spin(x2,y2,z
```

```
                    -1)
78              end if
79              !dE=Vspin*(intra+lambda*inter)+4
80              intra=(hidari+miggie+ue+shita)-(left+right+up+
                   down)
81              inter=(above2+below2)-(above1+below1)
82              Vspin=-2*spin(x1,y1,z)
83              !If boltzmann probability exp(-dE/T) is larger
                   than 1,
84              !then a trial is accepted. Even if this
                   probability
85              !is smaller than 1, a trial is accepted if this
                   quantity
86              !is larger than a random number.
87              if (rnd(0).le.w(Vspin,intra,inter)) then
88                 spin(x1,y1,z)=neutral2; spin(x2,y2,z)=
                      neutral1
89                 E=E+(Vspin*(intra+lambda*inter)+4)
90              end if
91           end if
92        end do
93     end subroutine Metropolis
```

Acknowledgements

I would like to thank Prof. S. Komura, Prof. D. Andelman, Prof. T. Kato, and Prof. S. Kumar for their useful discussions on this thesis. I acknowledge supports from Tokyo Metropolitan University Co-tutrial program and The Global Human Resource Program Bridging across Physics and Chemistry.

Bibliography

[1] B. Alberts, A. Johnson, P. Walter, J. Lewis, and M. Raff, *Molecular Biology of the Cell* (Garland Science, New York, 2008).

[2] G Schmitz and G Müller, J. Lipid Res. **32**, 1539 (1991).

[3] L. D. Frye and M. Edidin, *J. Cell Sci.* **7**, 319 (1970).

[4] S. J. Singer and G. L. Nicolson, *Science* **175**, 720 (1972).

[5] P. G. Saffman and M. Delbruck, *Proc. Nat. Acad. Sci. USA.* **72**, 3111 (1975).

[6] P. F. Almeida, *Biochim. Biophys. Acta.* **1788**, 72 (2009).

[7] D. A. Brown, *Annu. Rev. Cell. Dev. Biol.* **14**, 111 (1998).

[8] K. Simons and K. Ikonen, *Science* **290**, 1721 (2000).

[9] N. Chazal and D. Gerlier, *Microbiol. Mol. Biol. Rev.* **67**, 226 (2003).

[10] S. L. Veatch and S. L. Keller, *Biochim. Biophys. Acta* **1746**, 172 (2005).

[11] S. Komura and D. Andelman, *Adv. Coll. Int. Sci.* **208**, 34 (2014).

[12] L. Tayebi, Y. Ma, D. Vashaee, G. Chen, S. K. Sinha, and A. N. Parikh, *Nature Mater.* **11**, 1074 (2012).

[13] C. A. Stanich, A. R. Honerkamp-Smith, G. G. Putzel, C. S. Warth, A. K. Lamprecht, P. Mandal, E. Mann, T.-A. D. Hua, and S. L. Keller, *Biophys. J.* **105**, 172 (2013).

[14] L. Tayebi, A. N. Parikh, and D. Vashaee, *Int. J. Mol. Sci.* **14**, 3824 (2013).

[15] T. Hoshino, S. Komura, and D. Andelman, *J. Chem. Phys.* **143**, 243124 (2015).

[16] J. N. Israelachivili, *Intermolecular and Surface Forces* (Academic Press, New York, 2011).

[17] S. T. Milner and D. Roux, *J. Phys. I France* **2**, 1741 (1992).

[18] S. Komura and D. Andelman, *Europhys. Lett.* **64**, 844 (2003).

[19] K. W. Lee, *J. Kor. Phys. Soc.* **40**, L398 (2002).

[20] M. J. de Oliveira, R. B, Griffiths, *Surf. Sci.* **71**, 687 (1978).

[21] R. Pandit, M. Schick, and M. Wortis, *Phys. Rev. B* **26**, 5112 (1982).

[22] K. Kawasaki, *Phase Transitions and Critical Phenomena vol.2*, edited by C. Domb and M. S. Green (Academic Press, NewYork, 1972).

[23] D. P. Landau and K. Binder, *A Guide to Monte Carlo Simulations in Statistical Physics* (Cambridge Univ. Press, New York, 2009).

[24] X. T. Pham Phu, V. Thanh Ngo, and H. T. Diep, *Surface Science* **603**, 109 (2009).

[25] T. W. Capehart and M. E. Fisher, *Phys. Rev. B* **13**, 5021 (1976).

[26] L. Onsager, *Phys. Rev.* **65**, 117 (1944).

[27] K. Binder and E. Luijten, Phys. Rep. **344**, 179 (2001).

[28] L. L. Liu and H. E. Stanley, *Phys. Rev. Lett.* **29**, 927 (1972).

[29] M. Laradji and P. B. S. Kumar, *Phys. Rev. Lett.* **93**, 198105 (2004); *J. Chem. Phys.* **123**, 224902 (2005).

[30] S. Ramachandran, S. Komura, and G. Gompper, EPL **89**, 56001 (2010).

[31] A. J. Bray, *Adv. Phys.* **51**, 481 (2002).

[32] K. Binder and D. Stauffer, *Phys. Rev. Lett.* **33**, 1006 (1974).

[33] A. B. Bortz, M. H. Kalos, J. L. Lebowitz, and M. A. Zendejas, *Phys. Rev. B* **10**, 535 (1974).

[34] J. Marro, A. B. Bortz, M. H. Kalos, and J. L. Lebowitz, *Phys. Rev. B* **12**, 2000 (1975).

[35] M. Rao, M. H. Kalos, J. L. Lebowitz, and J. Marro, *Phys. Rev. B* **13**, 4328 (1976).

[36] K. Sornbundit, C. Modchang, N. Nuttavut, W. Ngamsaad, D. Triampo, and W. Triampo, *J. Kor. Phys. Soc.* **63**, 71 (2013).

[37] W. Ngamsaad, S. May, A. J. Wagner, and W. Triampo, *Soft Matter* **7**, 2848 (2011).

[38] A. Sur, J. Lebowitz, J. Marro, and M. Kalos, *Phys. Rev. B* **15**, 3014 (1977).